Naval Research Laboratory
Washington, DC 20375-5320

NRL/7320/MR—2021/8

Dependence of Submesoscale Eddy Distortion on Turbulent Mixing Schemes and It Effect on Boundary Layer Turbulence

YALIN FAN

ADAM RYDBECK

PRASAD THOPPIL

Ocean Dynamics and Prediction Branch
Ocean Science Division

December 3, 2021

REPORT DOCUMENTATION PAGE

Form Approved
OMB No. 0704-0188

1. REPORT DATE *(DD-MM-YYYY)*	**2. REPORT TYPE**	**3. DATES COVERED** *(From - To)*
03-12-2021	NRL Memorandum Report	

4. TITLE AND SUBTITLE

Dependence of Submesoscale Eddy Distortion on Turbulent Mixing Schemes and It Effect on Boundary Layer Turbulence

5a. CONTRACT NUMBER

5b. GRANT NUMBER

5c. PROGRAM ELEMENT NUMBER
62435N

6. AUTHOR(S)

Yalin Fan, Adam Rydbeck, and Prasad Thoppil

5d. PROJECT NUMBER
BE-435-040-6B63

5e. TASK NUMBER
BE-435-040

5f. WORK UNIT NUMBER
6B63

7. PERFORMING ORGANIZATION NAME(S) AND ADDRESS(ES)

Naval Research Laboratory
4555 Overlook Avenue, SW
Washington, DC 20375-5320

8. PERFORMING ORGANIZATION REPORT NUMBER

NRL/7320/MR--2021/8

9. SPONSORING / MONITORING AGENCY NAME(S) AND ADDRESS(ES)

Office of Naval Research
One Liberty Center
875 N. Randolph Street, Suite 1425
Arlington, VA 22203-1995

10. SPONSOR / MONITOR'S ACRONYM(S)

ONR

11. SPONSOR / MONITOR'S REPORT NUMBER(S)

12. DISTRIBUTION / AVAILABILITY STATEMENT

DISTRIBUTION STATEMENT A: Approved for public release; distribution is unlimited.

13. SUPPLEMENTARY NOTES

14. ABSTRACT

Different effect of the 6 OBL mixing models on the distortion of a submesoscale eddy and the corresponding responses of mixed layer dynamics are studied using stationary eddy experiments with NCOM and HYCOM. Generally, for the second moment turbulent closure models, the eddy mixed layer depth (MLD) is deeper in the Mellor-Yamada level 2.0 and 2.5 schemes but weakens much more quickly. The Ramsey-Harcourt and Kantha-Clayson schemes result in an eddy that is stronger and more coherent while characterized by a shallower mixed layer. In comparison to the second moment turbulent closure scheme, the KPP scheme produces weaker turbulent mixing with more symmetric structures and thus helps to better maintain the strength and coherence of the eddy.

The effect of submesoscale eddies on oceanic boundary layer turbulence was investigated through controlled numerical experiments conducted using the NCOM, HYCOM and the NCAR LES model with a moving eddy. The mixed layer dynamics and the variation of the MLD are very different at different locations relative to the eddy and between the HYCOM and LES simulations. Distinct dynamical processes are identified at different locations in the LES simulations. Along the center of the eddy, the turbulent field is dominated by strong shear production due to the geostrophic currents associated with the eddy, and the strong turbulent velocity fluctuations induced by the large horizontal shear brought by the eddy further act on the mean vertical shear to enhance the TKE and vertical mixing. On both sides of the eddy, the mixed layer dynamics are dominated by the combined effect of Ekman buoyancy flux and geostrophic shear. While Ekman buoyancy flux transports denser/lighter water over less/more dense water on the right/left hand side of the eddy and results in convectively unstable/stable state and destabilize/stabilize the water column, the presence of geostrophic shear that is aligned/oppose with the wind-driven shear can also augment/reduce the wind-driven TKE generation that occurs through mechanical shear production. Both processes lead to enhanced/reduced turbulence and deepening/shallowing of the mixed layer on the right/left-hand side of the eddy. These mixed layers behaviors are not observed in the HYCOM simulations because the KPP and GISS parameterization used in the model cannot represent the effect of horizontal gradients.

15. SUBJECT TERMS

Turbulent Mixing	Submesoscale eddy	Vertical coordinates	Turbulent closure models	Ocean boundary layer	NCOM
HYCOM	Large eddy simulation	KPP	COAMPS	ESPC	Langmuir turbulence

16. SECURITY CLASSIFICATION OF:			**17. LIMITATION OF ABSTRACT**	**18. NUMBER OF PAGES**	**19a. NAME OF RESPONSIBLE PERSON**
					Yalin Fan
a. REPORT	**b. ABSTRACT**	**c. THIS PAGE**	U	52	**19b. TELEPHONE NUMBER** *(include area code)*
U	U	U			(228) 688-4655

This page intentionally left blank.

Table of Contents

Listing of Figures ..... *iv*

Executive summary ..... *E*

I. Introduction *1*

II. Model Description *2*

II.1 NCOM **2**

II.2 HYCOM **2**

II.3 NCAR LES model **3**

II.4 The Large-scale Gradient Forcing **4**

III. Baroclinic Vortex Generation *5*

IV. Experiment design *7*

IV.1 Stationary Eddy **7**

IV.2 Moving Eddy **8**

V. Turbulent Mixing Models and Eddy Distortion *10*

V.I NCOM Experiments **10**

V.II HYCOM Experiments **15**

VI. Interaction Between Submesoscale Eddies and Ocean Boundary Layer Turbulence *20*

VI.1 Eddy distortion in the moving case **20**

VI.2 Mixed Layer Dynamics **25**

a. Along the center of the Eddy 27

b. On the Right-Hand Side of the Eddy 32

c. On the Left-Hand Side of the Eddy 35

VII. Summary *38*

Appendix A. Baroclinic Vortex Generation Code *39*

References: *42*

Listing of Figures

Figure IV.1. HYCOM Experimental design. ……9

Figure IV.2 (a) Sea surface temperature (SST), (b) sea surface height (SSH), (c) cross section of density (σ), and (d) cross section of current speed at the initial state of the imposed submesoscale eddy. ……10

Figure V.1 The vorticity (shading; $*10^{-4}$ s^{-1}) and currents (vectors) averaged from 0 – 15 meters are shown for the NCOM MLY simulation. The model simulation hour is shown in the upper left above each panel. Panels are a zoomed in view of the model domain to emphasize features of the eddy. ……11

Figure V.2 The vorticity (shading; $*10^{-4}$ s^{-1}) and currents (vectors) averaged from 0 – 15 meters are shown for the NCOM MLY25 simulation. The model simulation hour is shown in the upper left above each panel. Panels are a zoomed in view of the model domain to emphasize features of the eddy. ……12

Figure V.3 The vorticity (shading; $*10^{-4}$ s^{-1}) and currents (vectors) averaged from 0 – 15 meters are shown for the NCOM KC simulation. The model simulation hour is shown in the upper left above each panel. Panels are a zoomed in view of the model domain to emphasize features of the eddy. ……13

Figure V.4 The vorticity (shading; $*10^{-4}$ s^{-1}) and currents (vectors) averaged from 0 – 15 meters are shown for the NCOM HC simulation. The model simulation hour is shown in the upper left above each panel. Panels are a zoomed in view of the model domain to emphasize features of the eddy. ……14

Figure V.5 The temperature (shading; K) and salinity (contours; psu) are shown for the NCOM KC simulation. The respective eddy-tracking MLDs for each simulation are shown in the colored lines (red = HC, green = KC, yellow = MLY, blue = MLY25). ……15

Figure V.6 Time-depth evolution of (top) Temperature (°C) and (bottom) density (kg m^{-3}) from HYCOM simulation using (left) KPP and (right) GISS vertical mixing schemes from the stationary eddy experiment with spatially uniform wind-stress of 6×10^{-3} Pa. The mixed layer depth at the eddy center is plotted for KPP (solid line) and GISS (dashed line). The mixed layer depth is taken as the depth at which the density change equivalent to 0.5°C temperature decrease from the surface. The time in hours on x-axis. ……16

Figure V.7 Time-depth evolution of (top) Temperature (°C) and (bottom) density (kg m^{-3}) from HYCOM simulation using (left) KPP and (right) GISS vertical mixing schemes from the stationary eddy experiment with no surface forcing. The mixed layer depth at the eddy center is plotted for KPP (solid line) and GISS (dashed line). The mixed layer depth is taken as the depth at which the density change equivalent to 0.5°C temperature decrease from the surface. The time in hours on x-axis. ……17

Figure V.8 Time sequences of relative vorticity ($\times10^{-5}$ s^{-1}) starting 48 through 84 hours from the HYCOM simulations using stationary eddy (left) with spatially uniform surface wind-stress forcing (right) no surface forcing using the KPP mixing scheme. ……18

Figure V.9 Time sequences of relative vorticity ($\times 10^{-5}$ s^{-1}) starting from 48 through 84 hours from the HYCOM simulations using stationary eddy (left) with spatially uniform surface wind-stress forcing (right) no surface forcing using the GISS mixing scheme. ……19

Figure VI.1 Sea surface temperature (SST) at every 2 hour from hour 2 to 40 in the HYCOM run using the GISS mixing scheme. The white triangle in each panel indicates the location of point C. ……21

Figure VI.2 Sea surface temperature (SST) at every 2 hour from hour 42 to 80 in the HYCOM run using the GISS mixing scheme. The white triangle in each panel indicates the location of point C. The cyan circle in the hour 64 panel indicates the location of point D. ……22

Figure VI.3 Sea surface temperature (SST) at every 2 hour from hour 2 to 40 in the HYCOM run using the KPP mixing scheme. The white triangle in each panel indicates the location of point C. ……23

Figure VI.4 Sea surface temperature (SST) at every 2 hour from hour 42 to 80 in the HYCOM run using the KPP mixing scheme. The white triangle in each panel indicates the location of point C. The cyan circle in the hour 64 panel indicates the location of point D. ……24

Figure VI.5. Vertical profiles of potential temperature at point C in the HYCOM run with (a) KPP and (b) GISS schemes respectively. The green and blue solid lines in both panels represent the mixed layer depth in the KPP and GISS run respectively. The black thin lines are temperature contours at every 0.5 ^{o}C. ……25

Figure VI.6 Mixed layer depth (MLD) comparison at Points (a) A, (b) B, (c) C, (d) D, and (e) E among HYCOM experiments using the KPP (black) and GISS (blue) schemes, and LES experiments that is forced by HYCOM run using the KPP scheme (red) and GISS scheme (cyan). (f) Distance of the eddy center from point C in km in the HYCOM run using the KPP scheme. The green lines highlight the time when the eddy center passes point C. ……27

Figure VI.7 Potential density (σ_θ) and eddy viscosity (K_m) at Point C in the HYCOM simulation with KPP scheme and LES experiment LES_KPP1. The white solid line is the MLD in the experiment, and the white dashed lines indicate simulation hour 24, 34 and 48 respectively as marked. ……29

Figure VI.8 Eddy location relative to point C at simulation hour 24, 34, and 48. ……30

Figure 9. Normalized (a) TKE (e), (b) dissipation (ε), (c) shear production (ShearP), (d) pressure transport (PrsT), and (e) turbulent transport (TurT) at point C in simulation LES_KPP1. The black line is the MLD in the experiment, and the white dashed lines indicate simulation hour 24, 34 and 48 respectively as marked. ……31

Figure VI.10 Potential density (σ_θ) and eddy viscosity (K_m) at Point B in the HYCOM simulation with KPP scheme and LES experiment LES_KPP1. The white solid line is the MLD in the experiment, and the white dashed lines indicate simulation hour 24, 34 and 48 respectively as marked. ……33

Figure VI.11. Normalized (a) TKE (e), (b) dissipation (ε), (c) shear production (ShearP), (d) pressure transport (PrsT), and (e) turbulent transport (TurT) at point B in simulation LES_KPP1. The black line is the MLD in the experiment, and the white lines highlights the period when the center of the eddy passes the middle cross-section of the model domain. (f) Instant vertical velocity w at 20 m depth after 60 hours of model simulation ……34

Figure VI.12 Potential density (σ_θ) and eddy viscosity (K_m) at Point D in the HYCOM simulation with KPP scheme and LES experiment LES_KPP1. The white solid line is the MLD in the experiment, and the white dashed lines indicate simulation hour 24, 34 and 48 respectively as marked. ……36

Figure VI.13. Normalized (a) TKE (e), (b) dissipation (ε), (c) shear production (ShearP), (d) pressure transport (PrsT), and (e) turbulent transport (TurT) at point C in simulation LES_KPP1. The black line is the MLD in the experiment, and the white dashed lines indicate simulation hour 24, 34 and 48 respectively as marked. ……37

Executive summary

Different effect of the 6 OBL mixing models on the distortion of a submesoscale eddy and the corresponding responses of mixed layer dynamics are studied using stationary eddy experiments with NCOM and HYCOM. Generally, for the second moment turbulent closure models, the eddy mixed layer depth (MLD) is deeper in the Mellor-Yamada level 2.0 and 2.5 schemes but weakens much more quickly. The Ramsey-Harcourt and Kantha-Clayson schemes result in an eddy that is stronger and more coherent while characterized by a shallower mixed layer. In comparison to the second moment turbulent closure scheme, the KPP scheme produces weaker turbulent mixing with more symmetric structures and thus helps to better maintain the strength and coherence of the eddy.

The effect of submesoscale eddies on oceanic boundary layer turbulence was investigated through controlled numerical experiments conducted using the NCOM, HYCOM and the NCAR LES model with a moving eddy. The mixed layer dynamics and the variation of the MLD are very different at different locations relative to the eddy and between the HYCOM and LES simulations. Distinct dynamical processes are identified at different locations in the LES simulations. Along the center of the eddy, the turbulent field is dominated by strong shear production due to the geostrophic currents associated with the eddy, and the strong turbulent velocity fluctuations induced by the large horizontal shear brought by the eddy further act on the mean vertical shear to enhance the TKE and vertical mixing. On both sides of the eddy, the mixed layer dynamics are dominated by the combined effect of Ekman buoyancy flux and geostrophic shear. While Ekman buoyancy flux transports denser/lighter water over less/more dense water on the right/left hand side of the eddy and results in convectively unstable/stable state and destabilize/stabilize the water column, the presence of geostrophic shear that is aligned/oppose with the wind-driven shear can also augment/reduce the wind-driven TKE generation that occurs through mechanical shear production. Both processes lead to enhanced/reduced turbulence and deepening/shallowing of the mixed layer on the right/left-hand side of the eddy. These mixed layers behaviors are not observed in the HYCOM simulations because the KPP and GISS parameterization used in the model cannot represent the effect of horizontal gradients.

This page intentionally left blank

I. Introduction

Turbulent mixing plays an important role in the transport of momentum, heat, and particles across the mixed layer, and is critical to the vertical distribution of heat and salinity in the water column. Although the structure and physics of turbulent eddies can be directly simulated by direct numerical simulations or large-eddy simulations, it is too expensive and unrealistic to solve for the turbulence in geophysical models that require timely predictions of the flow fields over large domains such as those of Metzger et al. (2017) and Rowley et al. (2014). Thus, parameterizations are required to yield an idealized description of turbulence with a reasonable compromise between cost and accuracy. The K-profile parameterization (KPP) (Large et al., 1994) and second moment turbulent closure (SMTC) models are the two most popular types of approaches used to parameterize turbulence in the geophysical models. While many ocean models provide flexible choices of different turbulent mixing schemes for its users, whether and how these turbulent mixing models behave differently when interacting with the complicated submesoscale structures (horizontal length scales 1-10 km) in the ocean is not well understood.

In this report, we investigate the interaction mechanisms between the oceanic boundary layer turbulence and an idealized submesoscale eddy through controlled numerical experiments using the NCOM, HYCOM and the National Center for Atmospheric Research (NCAR) large eddy simulation (LES) model.

HYCOM and NCOM are the two principal ocean models that the Naval Oceanographic Office uses to provide detailed oceanic forecasts for navy operations. Tremendous efforts have been put into the development and improvement of these models. Several OBL mixing schemes are implemented in both models. Each of them represents a different approach to solve the turbulence in the water column and different stages of theory development. The K Profile parameterization (KPP) (Large et al., 1994) is an advanced surface boundary layer approximation with simple parameterizations to represent a range of mixing processes in the ocean interior. The estimates of the vertical mixing coefficients made by the KPP scheme are based on the surface boundary forcing and the state of the resolved velocity and potential density fields in the water column. The Mellor and Yamada (1974, 1982) closure models, MY2.0 and MY2.5, on the other hand, consider the energetics of the mixing explicitly by solving diagnostic and prognostic equations, respectively, for the turbulent kinetic energy (TKE) and turbulent length scale. The prognostic equations used for the MY2.5 model carry information about the time history of the turbulence and can account for both advection and diffusion of TKE. The NASA GISS model (Canuto et al., 2001) improved the MY2.0 model's treatment of pressure correlations, added non-local third-order moments, and extended the resolved mixing below the mixed layer. Kantha and Clayson (2004) added vortex forcing to the MY2.5 model to represent the effect of Langmuir turbulence. Harcourt (2015) further improved the Kantha & Clayson model and incorporated the vortex forcing in the stability equations as well. In this work, the performance of these turbulent mixing models will be evaluated against the LES model, and the differences in their behavior will be investigated.

Manuscript approved December 1, 2021.

II. Model Description

II.1 NCOM

The Navy Coastal Ocean Model (NCOM) Version 4.1, based on the Princeton Ocean Model (Blumberg and Mellor 1983; Blumberg and Mellor 1987) and the Sigma/*Z*-level Model (Martin et al., 1998), has a free-surface and is built on the primitive equations and the hydrostatic, Boussinesq, and incompressible approximations. The Mellor Yamada Level 2 (MYL2), MYL2.5, Kantha-Clayson, and Ramsey-Harcourt turbulence models are provided for the parameterization of vertical mixing. The vertical mixing enhancement scheme of Large et al. (1994) is also offered for parameterization of unresolved mixing processes occurring at near-critical Richardson numbers.

The model uses a staggered Arakawa C grid with spatial finite differences that are mostly second-order centered. The temporal scheme is leapfrog, with an Asselin filter to suppress time-splitting. Most terms are treated explicitly in time, but the propagation of surface waves and vertical diffusion are treated implicitly. NCOM 4.1 has two choices of vertical grid, which are selected at compile time, the hybrid sigma & z-level grid and the general vertical coordinate. We use the original vertical grid used by NCOM, which is a hybrid sigma and z-level grid with sigma coordinates used from the surface down to a specified depth and level coordinates used below the specified depth. The switch from sigma to level coordinates can occur at any specified interface between layers, i.e., from just below the uppermost layer (there must be at least one sigma layer at the surface) to the bottom of the lowest layer (in which case the entire grid would be sigma coordinate). On the sigma coordinate portion of the grid, each sigma layer is a fixed fraction of the depth from the surface to the bottom of the sigma coordinate grid. On the level portion of the grid, each layer's depth and thickness is fixed and the bottom depth is adjusted to match the depth of the nearest layer.

The NCOM surface boundary conditions are the surface stress for the momentum equations, the surface heat flux for the temperature equation, and the effective surface salt flux for the salinity equation. The bottom boundary conditions are the bottom drag for the momentum equations, which is parameterized by a quadratic drag law, and zero flux for the temperature and salinity equations. The evolution of the NCOM simulations is relatively insensitive to the precise formulation of the bottom boundary, as revealed in many sensitivity tests using various bottom drags and free-slip conditions. Surface stress forcing and surface heat flux are specified and invariant in time and space over the NCOM domain for the idealized simulations performed in this study.

II.2 HYCOM

HYCOM is a primitive equation general ocean circulation model applied to large scale, marginal sea, and coastal studies. A more complete description of HYCOM physics can be found in Bleck (2002). HYCOM solves five prognostic equations: two for horizontal velocity components, a mass continuity equation, and two conservative equations that govern temperature and salinity. The prognostic equations are time-integrated using a split-explicit treatment of barotropic and baroclinic modes. It employs potential density referenced to 2000 m and includes effects of thermobaricity (Chassignet et al., 2003).

HYCOM uses a mixture of vertical coordinates, hence the HYbrid as part of its name. Vertical coordinates can be (1) isopycnals (density tracking), often the best coordinate in the deep stratified

ocean; (2) levels of equal pressure (nearly fixed depths), best used in the mixed layer and unstratified ocean; and (3) sigma-levels (terrain following), often the best choice in shallow water. HYCOM combines all three approaches by choosing the optimal distribution at every time step. The model makes a dynamically smooth transition between coordinate types by using the layered continuity equation. The hybrid coordinate extends the geographic range of applicability of traditional isopycnic coordinate circulation models toward shallow coastal seas and unstratified parts of the world ocean. It maintains the significant advantages of an isopycnal model in stratified regions while allowing more vertical resolution near the surface and in shallow coastal areas, hence providing a better representation of the upper ocean physics. HYCOM is configured with options for a variety of mixed layer submodels (Halliwell, 2004) K-Profile Parameterization (Large et al., 1994), GISS (NASA Goddard Institute for Space Studies level 2), which is constructed using the Reynolds stress model (Canuto et al., 2001, 2002) and Mellor-Yamada mixing.

II.3 NCAR LES model

The LES model used in this study was first introduced by McWilliams et al. (1997) to solve the flow components using the wave-phase-averaged Craik–Leibovich theory (e.g., Craik and Leibovich 1976; Suzuki and Fox-Kemper 2016) with the effect of wave on current through the vortex force, Stokes-Coriolis force, Lagrangian mean advection associated with Stokes drift, and a wave-averaged increment to pressure that arises through conservative wave–current interactions.

The filtered Craik-Leibovich momentum equation is given as (McWilliams et al. 1997)

$$\frac{D\vec{u}}{Dt} + f\vec{z} \times (\vec{u} + \vec{u}_{st}) = -\nabla\pi - g\vec{z}(\rho/\rho_0) + \vec{u}_{st} \times \vec{\omega} + SGS, \quad (1)$$

where g is the gravitational acceleration, $D/Dt = \partial_t + \vec{u} \cdot \nabla$, $\vec{u}$ (u, v, w) is the current velocity vector, $\vec{u}_{st}$ (u_{sx}, u_{sy}) is the Stokes drift vector, and $\pi = p/\rho_0 + \frac{1}{2}[|\vec{u} + \vec{u}_{st}|^2 - |\vec{u}|^2]$ is a generalized pressure.

The temperature and salinity equations are given as

$$\frac{DT}{Dt} + \vec{u}_{st} \cdot \nabla T = \mathrm{SGS} + \frac{1}{C_p}\frac{\partial I}{\partial z} \quad (2)$$

$$\frac{DS}{Dt} + \vec{u}_{st} \cdot \nabla S = \mathrm{SGS} \quad (3)$$

where T is temperature, S is salinity, $C_p = 4.1 \times 10^6 Jm^{-3}K^{-1}$ is the specific heat of seawater per unit volume, and I is the net surface heat flux. The surface freshwater flux term is omitted because there is no precipitation during the study period and the surface evaporation is negligible.

The details on the subgrid scale model, which is only schematically indicated as SGS here in equations (1) to (3) can be found in Sullivan et al (2007), who has introduced the Stokes production into the SGS model. The conservative wave-induced additional diffusivity (e.g., McWilliams et al., 2004; Uchiyama et al. 2010) is insignificant compared with other diffusivity sources and thus ignored in our model. The dynamical equations are integrated in time using third-order Runge-Kutta methods. Horizontal derivatives are evaluated with Fourier pseudo-spectral method. Vertical derivatives are approximated with a high-resolution scheme with flux limiter to suppress spurious oscillation. (e.g., Sullivan et al. 1996 and Sullivan and Patton 2011). The model has been shown

to accurately reproduce observed upper ocean responses to a variety of meteorological conditions (e.g., Kukulka et al., 2009; Liang et al., 2017; Fan et al., 2018; Fan et al., 2020).

The model domain is set to be rectangular in three dimensions with 300 m x 300 m in the horizontal and 200 m in vertical directions. There were 250 grid points in both horizontal directions with a uniform spacing of 1.2 m. The vertical grid was stretched with a smallest spacing of 0.2 m near the surface to better resolve the boundary layer turbulence (McWilliams et al., 2014). Periodic boundary conditions are specified for the horizontal directions, outward wave radiation and zero stress are set for the bottom, and no-normal flow and specified momentum and heat fluxes are applied at the surface.

II.4 The Large-scale Gradient Forcing

Due to the high computational cost, LES studies are usually limited to a finite domain with hundreds of meters in each horizontal direction and, as a result, cannot resolve large-scale flows. Most of these LES models such as the NCAR LES use periodic boundary conditions in the horizontal directions, which assumes the physical properties (i.e. temperature and salinity) and expected flow patterns in the area of interest are of a periodically repeating nature so that the small LES domain is representative of a larger area. Such treatment of boundary conditions significantly reduces the computational cost, but at the same time places serious limitations on predicting turbulence within inhomogeneous flow fields, especially those strongly influenced by submesoscale features. To study effects of submesoscale eddies on oceanic boundary layer turbulence, large-scale gradient forcing (LSGF) is introduced following Wang et al. (1998). Computational constraints preclude the possibility of a 2-way coupling of the LES model with a general ocean circulation model. Therefore, a one-way interaction approach is adopted. The underlying assumption is the scale separation hypothesis. It states that the horizontal scales of the large-scale temperature and salinity fluxes are much larger than the scales of motions that are contained within the domain of the LES model, such that the horizontal derivatives of the large-scale terms are unaffected by small-scale motions. By doing so, we can account for the large scale influence on the small scale turbulence while still keeping the periodic boundary condition. The advantage for this approach is that there is no need to impose vertical profiles of velocities, temperature and salinity as horizontal boundary conditions, which may cause wave reflections at the lateral boundaries and interfere with small-scale turbulent motions inside the model domain.

The modified temperature and salinity equations are given as

$$\frac{DT}{Dt} + \vec{u}_{st} \cdot \nabla T = \mathrm{SGS} + \frac{1}{C_p}\frac{\partial I}{\partial z} - \left(u\frac{\partial \bar{T}^L}{\partial \bar{x}^L} + v\frac{\partial \bar{T}^L}{\partial \bar{y}^L}\right) + \nabla_h \cdot \overline{u'T'} \tag{4}$$

$$\frac{DS}{Dt} + \vec{u}_{st} \cdot \nabla S = \mathrm{SGS} - \left(u\frac{\partial \bar{S}^L}{\partial \bar{x}^L} + v\frac{\partial \bar{S}^L}{\partial \bar{y}^L}\right) + \nabla_h \cdot \overline{u'S'} \tag{5}$$

The terms in the parentheses on the right-hand side of equations (4) and (5) are the large-scale interaction terms for temperature and salinity, with the overbar and superscription L (i.e. $\bar{T}^L$) stands for large-scale motions. The last term in these two equations represents the eddy forcing for temperature and salinity.

The modified momentum equation is given as:

$$\mathbf{u}_t + \mathbf{u}\cdot\nabla\mathbf{u} + 2\boldsymbol{\Omega}\times(\mathbf{u}+\mathbf{u}_s) = -\nabla\pi - g\left({}^{\rho}/_{\rho_0}\right) + \mathbf{u}_s\times\omega + \mathbf{G} \qquad (6)$$

Where term G added at the end of the right-hand side of the equation represents the large-scale interaction terms with three components:

$$G_u = -u\frac{\partial\bar{u}^L}{\partial x} - v\frac{\partial\bar{u}^L}{\partial y} - \bar{w}^L\frac{\partial u}{\partial z} - \frac{1}{\rho}\frac{\partial\bar{p}^L}{\partial x} - \nabla\cdot E_x \qquad (6a)$$

$$G_v = -u\frac{\partial\bar{v}^L}{\partial x} - v\frac{\partial\bar{v}^L}{\partial y} - \bar{w}^L\frac{\partial v}{\partial z} - \frac{1}{\rho}\frac{\partial\bar{p}^L}{\partial y} - \nabla\cdot E_y \qquad (6b)$$

$$G_w = -u\frac{\partial\bar{w}^L}{\partial x} - v\frac{\partial\bar{w}^L}{\partial y} - \bar{w}^L\frac{\partial w}{\partial z} \qquad (6c)$$

The last term in equations (6a) and (6b) represent the momentum components of the eddy forcing, and are calculated as the divergence of the eddy stress tensor according to Plumb (1986):

$$\nabla\cdot\boldsymbol{E} = \hat{\mathbf{k}}\times\overline{\boldsymbol{q}'\boldsymbol{u}'}, \qquad with \quad \boldsymbol{E} = \begin{pmatrix} -M+P & N & 0 \\ N & M+P & 0 \\ -S & R & 0 \end{pmatrix} \qquad (7)$$

where $\boldsymbol{u}'(u',v')$ is the velocity fluctuation in the large scale flow, $\boldsymbol{q}'(q_x,q_y)$ is the vorticity, $M = \frac{\overline{v'^2-u'^2}}{2}$ and $N = -\overline{u'v'}$ are the Reynolds stresses, $P = \frac{\overline{b'^2}}{2N_0^2}$ is eddy potential energy, and $R = \frac{f_0}{N_0^2}\overline{u'b'}$ and $S = \frac{f_0}{N_0^2}\overline{v'b'}$ are eddy buoyancy fluxes or eddy form stresses.

III. Baroclinic Vortex Generation

The development of a subroutine to generate an idealized baroclinic vortex within the NCOM initial conditions greatly benefited from previous work documented in Penven et al. (2006) as well as Spall and Holland (1991). This implementation also benefited from recent modifications by NRL scientist Jie Yu for a separate project investigating 2-way grid interactions in NCOM. In short, we generate a geotropically balanced baroclinic vortex in an idealized ocean on an f-plane. The vortex is defined by a warm temperature anomaly at the surface that exponentially decays downward in the water column and is in dynamically equilibrium with the free surface and 3D velocity. The vortex subsequently evolves freely in the simulation over a 5-day period. A brief summary of this setup and related equations are documented below.

The formation of the eddy may be described using a top-down approach, with the prescription of the surface pressure field occurring first. The surface dynamic pressure distribution in Penven et al. (2006) is defined as a Gaussian function using the following equation:

$$P(x,y,0) = P_0(x,y)e^{-\frac{x^2+y^2}{2\lambda^2}} \qquad (8)$$

where λ is the horizontal e-folding scale (400 m). P_0 is defined by the maximum geostrophic velocity using the following equation:

$$P_0 = \rho_0 f_0 u_{max} \lambda \sqrt{e} \quad (9)$$

where ρ_0 is the mean surface density (1025.0 kg m^{-3}), $f_0$is the Coriolis parameter at 10.0N ($1.27*10^{-5}$ rad s^{-1}), and u_{max} is the maximum geostrophic velocity (1.0 m s^{-1}).

Following Penven et al. (2006), the baroclinic vortex is defined in the presence of a continuous background stratification with no motion below a specified level (z = -H1). As a result, the dynamic pressure as a function of depth is may be written as:

$$P(x,y,z) = F(x,y,z)e^{-\frac{x^2+y^2}{2\lambda^2}} \quad (10)$$

and the upper and lower bounds of $P(x,y,z)$ are defined such that:

$$F(x,y,0) = P_0 \quad (11)$$

$$F(x,y,-\mathrm{H1}) = 0. \quad (12)$$

The density field should also be uniform at and below -H1 to ensure there is no horizontal motion. An additional constraint by Penvent et al. (2006) is imposed such that the density anomaly that relates to the dynamic pressure via the hydrostatic balance should also disappear at and below the specified level (-H1). To do this, the following formula must also be satisfied:

$$\frac{\partial F(x,y,-\mathrm{H1})}{dz} = 0. \quad (13)$$

The following solution which satisfied these constraints is provided by Penvent et al. (2006):

$$P(x,y,z) = P_0 \frac{\mathrm{H1}-1+z+e^{-(z+\mathrm{H1})}}{\mathrm{H1}-1+e^{-\mathrm{H1}}} e^{-\frac{x^2+y^2}{2\lambda^2}} \quad (14).$$

By adding a density anomaly to the background linear stratification, Penvent et al. (2006) defined the total density as:

$$\rho(x,y,z) = \begin{cases} \rho_0 - \frac{\rho_0 N^2}{g} z - \frac{P_0}{g} \frac{1-e^{-(z+\mathrm{H1})}}{\mathrm{H1}-1+e^{-\mathrm{H1}}} e^{-\frac{x^2+y^2}{2\lambda^2}}, & z > -\mathrm{H1} \\ \rho_0 - \frac{\rho_0 N^2}{g} z, & x \leq -\mathrm{H1} \end{cases} \quad (15).$$

NRL scientists Jie Yu modified this function such that fields are more continuous near the level of no motion, and we have adopted this improvement in our study. The modified solution is written as:

$$P(x,y,z) = P_0 e \left(\frac{z}{\mathrm{H1}} + e^{-(1+z/\mathrm{H1})} \right) e^{-\frac{x^2+y^2}{2\lambda^2}} \quad (16)$$

Using equation (9), the density may be written as

$$\rho(x,y,z) = \begin{cases} \rho_0 - \frac{\rho_0 N^2}{g} z - \frac{P_0}{g} \frac{e}{\mathrm{H1}} \left(1 - e^{-(1+z/\mathrm{H1})} \right) e^{-\frac{x^2+y^2}{2\lambda^2}}, & z > -\mathrm{H1} \\ \rho_0 - \frac{\rho_0 N^2}{g} z, & x \leq -\mathrm{H1} \end{cases} \quad (17).$$

We use the modified functions in our simulations to define the baroclinic vortex. As a result, the sea surface height, zonal currents, and meridional currents are described by:

$$ssh(x,y) = \frac{P_0 e^{-\frac{x^2+y^2}{2\lambda^2}}}{\rho_0 g - \frac{e-1}{\mathrm{H1}} P_0 e^{-\frac{x^2+y^2}{2\lambda^2}}} \quad (18)$$

$$u(x,y,z) = \frac{-1}{f\rho_0}\frac{\partial P(x,y,z)}{\partial y} \quad (19)$$

$$v(x,y,z) = \frac{1}{f\rho_0}\frac{\partial P(x,y,z)}{\partial x} \quad (20).$$

The temperature is related to the density through a simple linear relation and the salinity increases monotonically with depth until reaching the level of no motion. Temperature (T) and salinity (S) are defined using the following equations:

$$T(x,y,z) = (1030.0 - \rho(x,y,z))/0.28 \quad (21)$$

$$S(x,y,z) = 33.0 - 0.008 * z \quad (22)$$

Excerpt of Fortran code that prescribes these variables are given in Appendix A for interested users.

IV. Experiment design

IV.1 Stationary Eddy

Stationary eddy experiments are conducted to investigate the effect of different turbulent closure models on eddy distortion.

For NCOM stationary eddy simulations, the horizontal domain size is 600 km x 600 km with 1 km grid spacing. Initial tests revealed that results are insensitive to the use of doubly periodic boundary conditions versus boundary conditions specified to the initial conditions with a lateral relaxation timescale applied to velocities and scalars. The rather large horizontal domain size of the model sufficiently distances lateral boundary effects from the eddy evolution at the model center, regardless of their formulation. The vertical grid extends from the surface to 500 m in depth, with 101 vertical levels. The vertical grid is exponentially stretched to the bottom such that grid spacings increase with depth. The upper ocean has a grid spacing of ~0.5 m while layers near the bottom have thickness of ~15m. Vertical layers near the mixed layer depth (25 – 50 m) have vertical grid spacings of ~1.5 – 2.5 m. Sensitivity tests were also performed to determine the impact of bottom roughness on eddy evolution. Switching from a free-slip bottom boundary condition to one with a large bottom roughness value resulted in no discernible differences in the eddy evolution. This adds confidence that the idealized eddy evolution in the upper ocean is not sensitive to the exact prescription of the bottom boundary in NCOM over the 5-day model integration period.

Atmospheric forcing of NCOM is uniformly prescribed with an westerly zonal wind stress of $6.0*10^{-3}$ Pa and no surface heat and freshwater fluxes. No relaxation of vectors and scalars to climatological values are applied anywhere in the water column. The simulations are allowed to

freely evolve from the initial conditions and atmospheric forcing. Horizontal diffusion is also removed such that the role of vertical mixing features more prominently in the evolution of the baroclinic eddy. The focus of the NCOM model simulations is on the role of vertical mixing scheme in modulating the evolution of the baroclinic vortex. Because of this, we performed individual simulations for MLY, MLY2.5, KC, and HC mixing schemes in NCOM. A zonal Stokes drift that exponentially decays with depth is prescribed in the simulations using the KC and HC mixing schemes. Assuming a Langmuir number of 0.3, the surface Stokes drift is calculated from the surface friction velocity using the following equation:

$$U_{SD}(x, y, 0) = \frac{\sqrt{6.0*10^{-6}\mathrm{m}^2\ \mathrm{s}^{-2}}}{0.3^2} \tag{23}$$

The zonal Stokes drift as a function of depth is defined as:

$$U_{SD}(x, y, z) = U_{SD}(x, y, 0)e^{\frac{2\pi}{L}z} \tag{24}$$

where L is the wavelength (60 m) and U_{SD} is the Stokes Drift with a surface value of -2.72*10^{-2} m s^{-1}.

For HYCOM idealized eddy simulations, the horizontal domain size is 540 km x 540 km with 1 km grid spacing. There are 122 hybrid layers in the vertical with 1 m resolution in the upper 50 m guided by LES simulations. The layer structures are derived from the current operational HYCOM (41 layers) with additional enhancements in the upper ocean. It employs potential density referenced to 2000 m and includes effects of thermobaricity (Chassignet et al., 2003). A double periodic boundary conditions are used. The larger domain minimized the lateral boundary effects from interfering with the evolution of the eddy. A flat bottom at 450 m is prescribed. The HYCOM is initialized from temperature, salinity and velocity values that are representative of a submesoscale eddy. The model is integrated forward for 7 days with 60 s baroclinic and 6 s barotropic time-step. The surface forcing of HYCOM simulations include spatially uniform easterly zonal wind-stress of 6.0*10^{-3} Pa and no heat and freshwater flux forcing are prescribed. To understand the sensitivity of the various vertical mixing schemes on the evolution of submesoscale eddy, HYCOM simulations employed KPP and GISS mixing schemes (HYCOM simulation using MY produced instabilities and not shown here). HYCOM simulations are performed for moving and stationary idealized cases. For stationary eddy experiments, an additional experiment is performed in which no wind-stress surface forcing is prescribed. The horizontal gradient and eddy forcing terms are calculated which is used as lateral boundary conditions for LES simulations.

IV.2 Moving Eddy

Idealized HYCOM and LES simulations are conducted to investigate the interaction between submesocale eddies and ocean boundary layer turbulence with a moving eddy.

Figure IV.1 illustrates our experimental design. The HYCOM domain is set up to be 540 km by 540 km in the horizontal direction with 1 km resolution, and 450 m in the vertical direction with 122 layers. 1m resolution was used for the top 50 meters. Stretched grids are used below 50 meters with the thickest layer of 27.5 m near the bottom. Periodic boundary conditions are specified for the horizontal directions, outward wave radiation and zero stress are set for the bottom.

Stratified ocean initial conditions are prescribed for the idealized experiments with a constant density layer from the surface to a depth of 20 m. Below that layer, stable stratification of $d\theta/dz$ = 0.01 K/m is prescribed with the thermal expansion coefficient α = 2 x10^{-4} K^{-1}. Weak constant wind forcing is applied at the ocean surface for all experiments with wind stress τ = 0.037 N m^{-2} (corresponding to a wind speed of about 5 m s^{-1}), No heat flux is used.

An idealized submesoscale eddy is generated using gaussian surface pressure distribution as described in section III, and imposed to the HYCOM model domain with the eddy center position to be 25 km away from the domain center (point C). The initial eddy maximum surface current is set to be 1 m s^{-1} with a maximum temperature anomaly of 1.5°C. The vertical eddy decay scale is ~300 m. The initial state of sea surface temperature (SST), sea surface height (SSH), cross section of density (σ) and current speed of the imposed eddy are given in Figure IV.2 for illustration.

Five locations from A to E along the middle cross section of the model domain positioned at 10 km away from each other are selected for the detailed analysis of model results . Two HYCOM simulations were conducted using the KPP and GISS mixing schemes respectively.

Corresponding LES simulations were conducted at the five locations using the large scale gradient forcing and eddy forcing calculated form the HYCOM simulations as described in section II.4. The LES simulations using large scale forcing calculated from HYCOM run with the GISS and KPP schemes are documented in experiment LES_GISS and LES_KPP respectively.

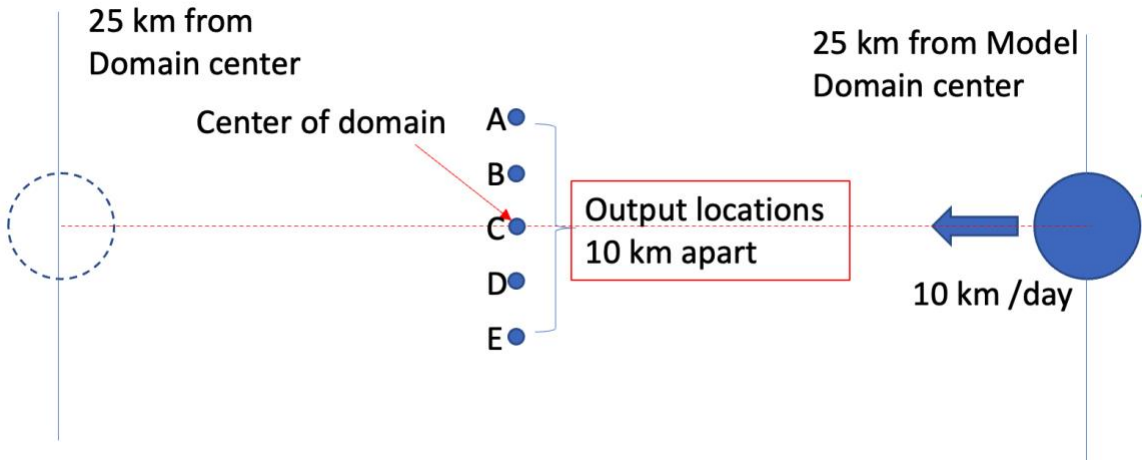

Figure IV.1. HYCOM Experimental design.

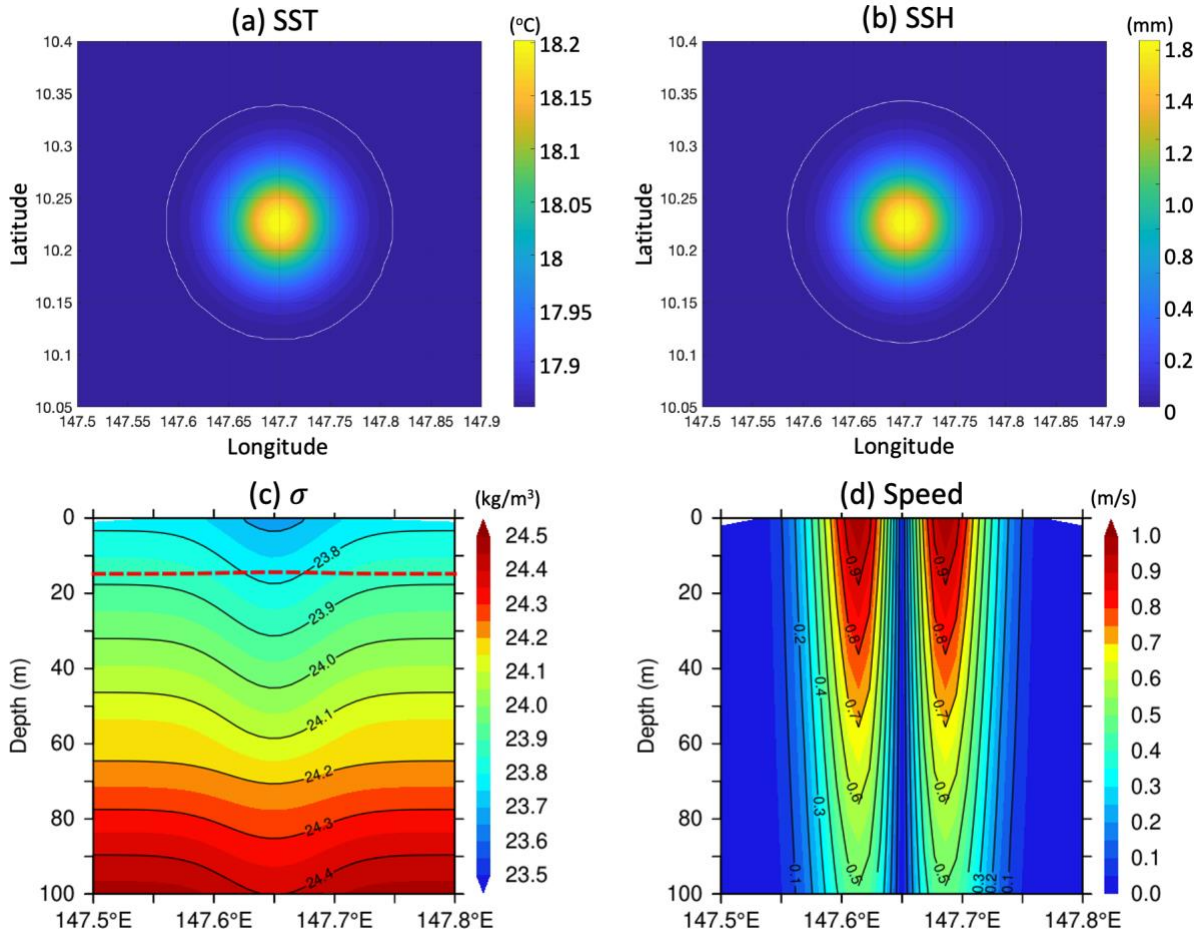

Figure IV.2 (a) Sea surface temperature (SST), (b) sea surface height (SSH), (c) cross section of density (σ), and (d) cross section of current speed at the initial state of the imposed submesoscale eddy.

V. Turbulent Mixing Models and Eddy Distortion

V.I NCOM Experiments

Several NCOM simulations were performed to investigate the sensitivity of the idealized eddy evolution to the mixing parameterization. The eddy was initialized with a maximum surface current specified to 1 m/s and an ocean state initialized with zero background current velocities. The parameterizations tested in NCOM included the MLY, MLY25, KC, and HC mixing schemes. A uniform Stokes drift was applied for the KC and HC mixing schemes, as described in the earlier NCOM model setup section. The results are described below.

In the NCOM MLY and MLY25 simulations, the eddy weakened considerably during the 5-day model integration period as observed in figure V.1 and V.2. Given the same atmospheric forcing and background ocean conditions, the eddy evolution between MLY and MLY25 is quite similar, with only slight differences observed in the vorticity and current field. Noticeable

asymmetries in the vorticity field begin to develop around 36 hours, associated with strong deformations in the flow in the following days. As will be shown later, the systematic weakening of vorticity occurs more rapidly in the MLY and MLY25 simulations when compared to the KC and HC simulations. This suggests that the MLY and MLY25 vertical mixing schemes are much more effective at propagating vorticity away from the eddy center near the ocean surface. This is also confirmed later when examining the mixed layer depths (MLD) at the eddy center between the respective model simulations.

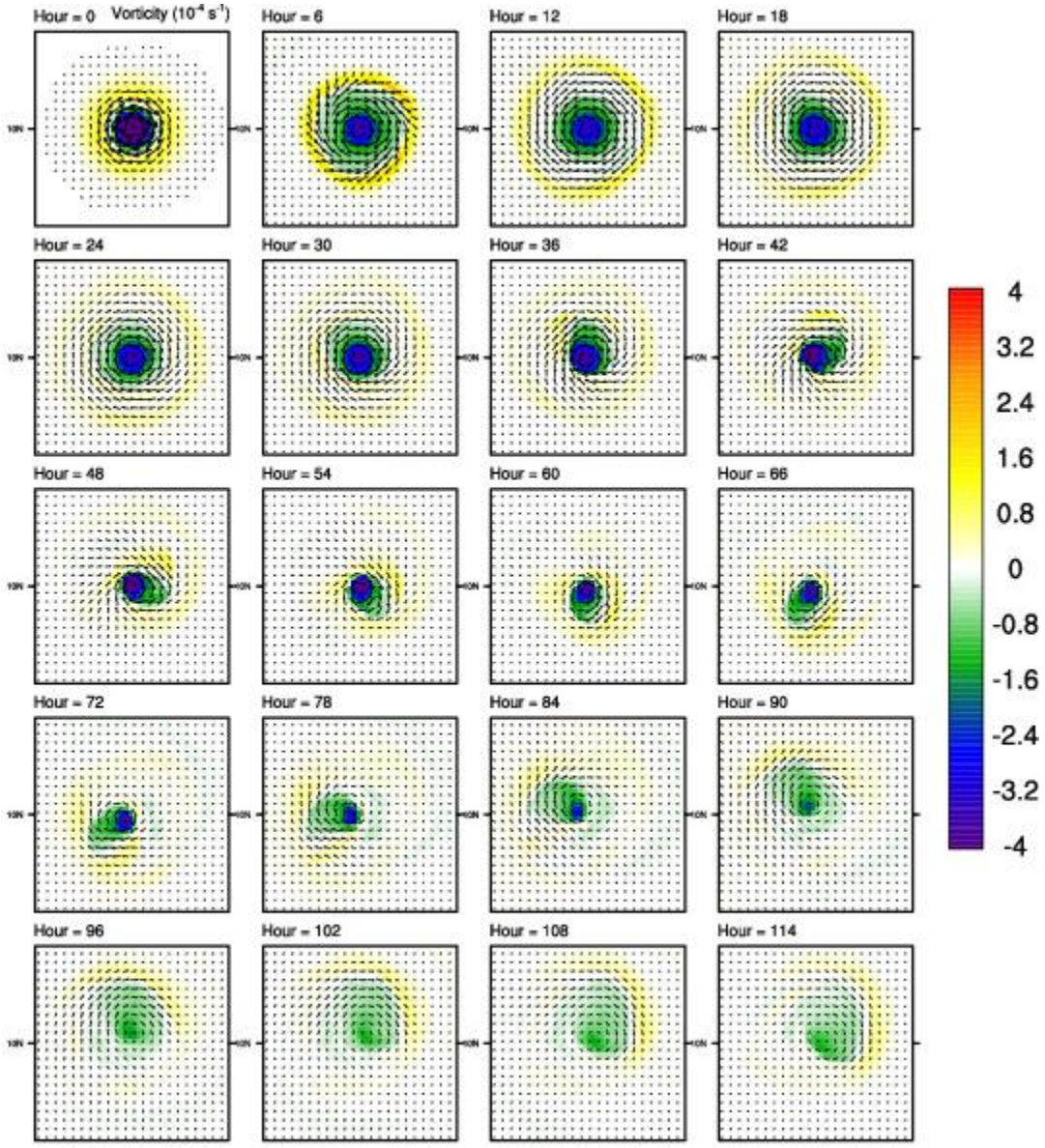

Figure V.2 The vorticity (shading; $*10^{-4}$ s^{-1}) and currents (vectors) averaged from 0 – 15 meters are shown for the NCOM MLY simulation. The model simulation hour is shown in the upper left above each panel. Panels are a zoomed in view of the model domain to emphasize features of the eddy.

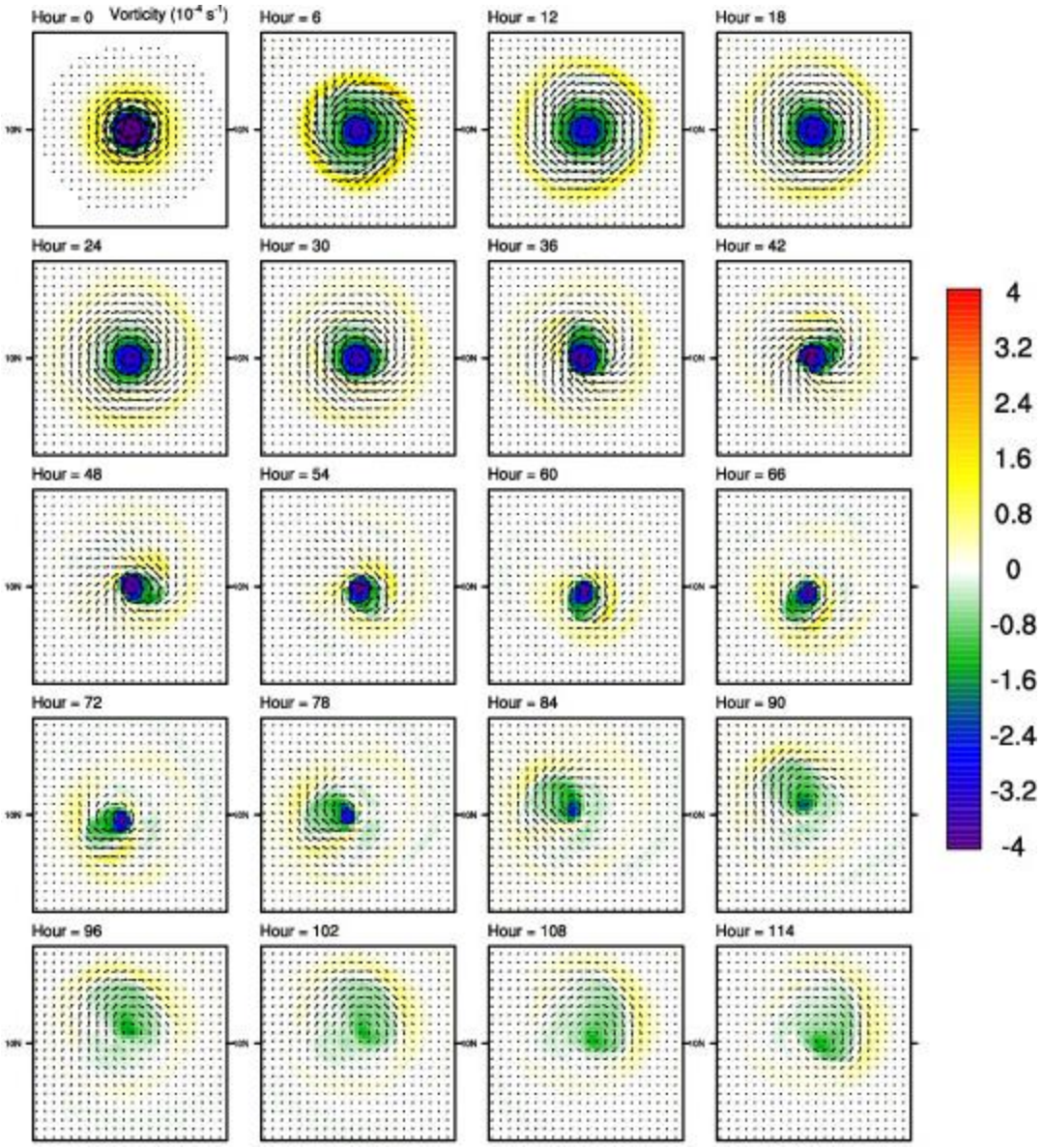

Figure V.2 The vorticity (shading; $*10^{-4}$ s^{-1}) and currents (vectors) averaged from 0 – 15 meters are shown for the NCOM MLY25 simulation. The model simulation hour is shown in the upper left above each panel. Panels are a zoomed in view of the model domain to emphasize features of the eddy.

The HC and KC mixing schemes results in a stronger eddy at the end of the 5-day model integration period (figures V.3 and V.4). The eddy also remains quasi-axisymmetric until hour 78, when the broader envelope of vorticity begins to deflect to the northeast and gradually rotates clockwise around the eddy. This delay in deformation in the eddy requires approximately double the time as the MLY and MLY25 simulations, indicating that the HC and KC mixing schemes help maintain the coherent eddy structure for longer. This results in an overall stronger eddy as well. A possible explanation for this behavior is that vertical shear created by the Stokes drift that is prescribed in the HC and KC mixing schemes creates horizontal vorticity that is tilted in the vertical, mitigating the vorticity dampening effects present in the MLY and MLY25 simulations.

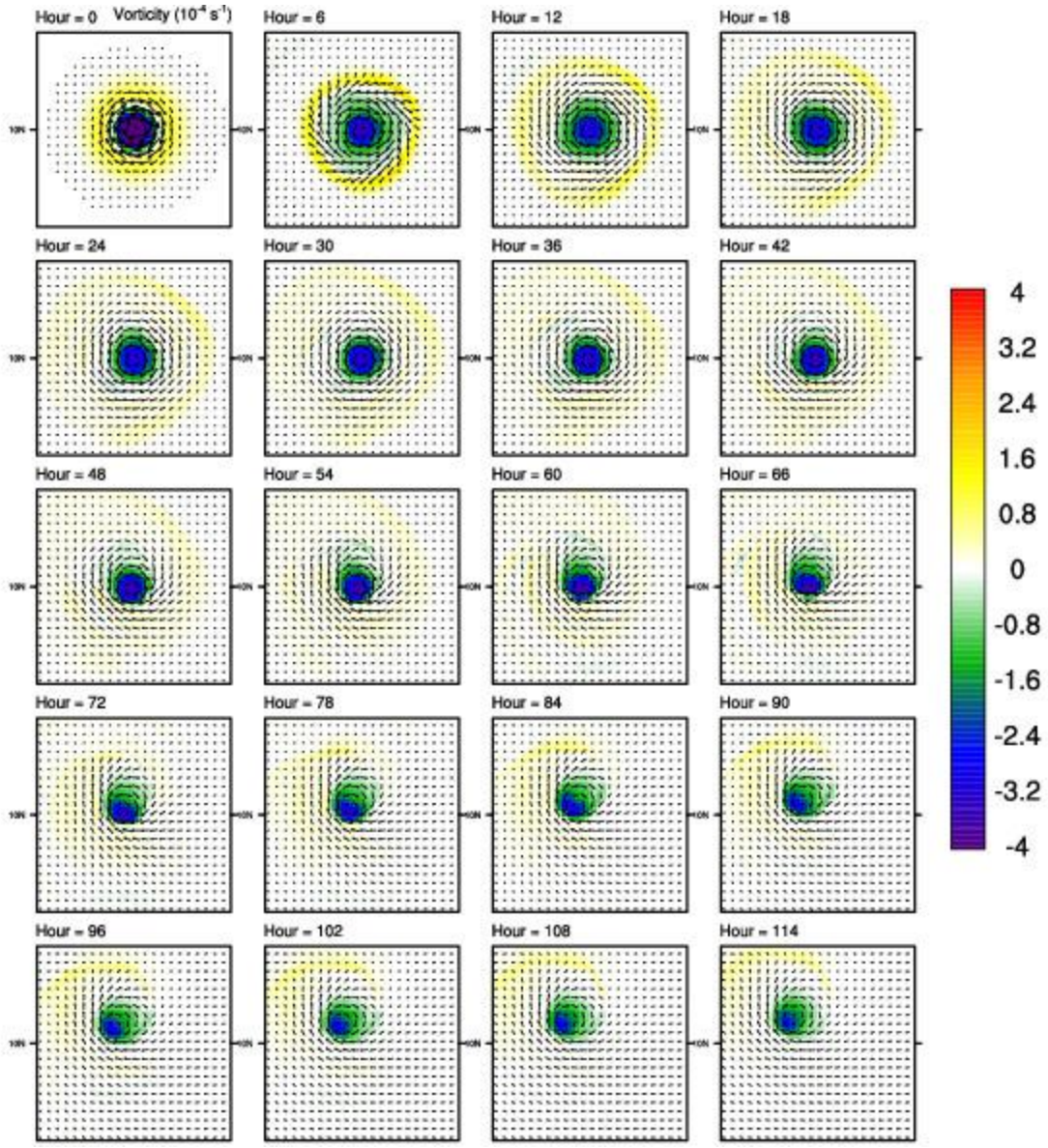

Figure V.3 The vorticity (shading; $*10^{-4}\,s^{-1}$) and currents (vectors) averaged from 0 – 15 meters are shown for the NCOM KC simulation. The model simulation hour is shown in the upper left above each panel. Panels are a zoomed in view of the model domain to emphasize features of the eddy.

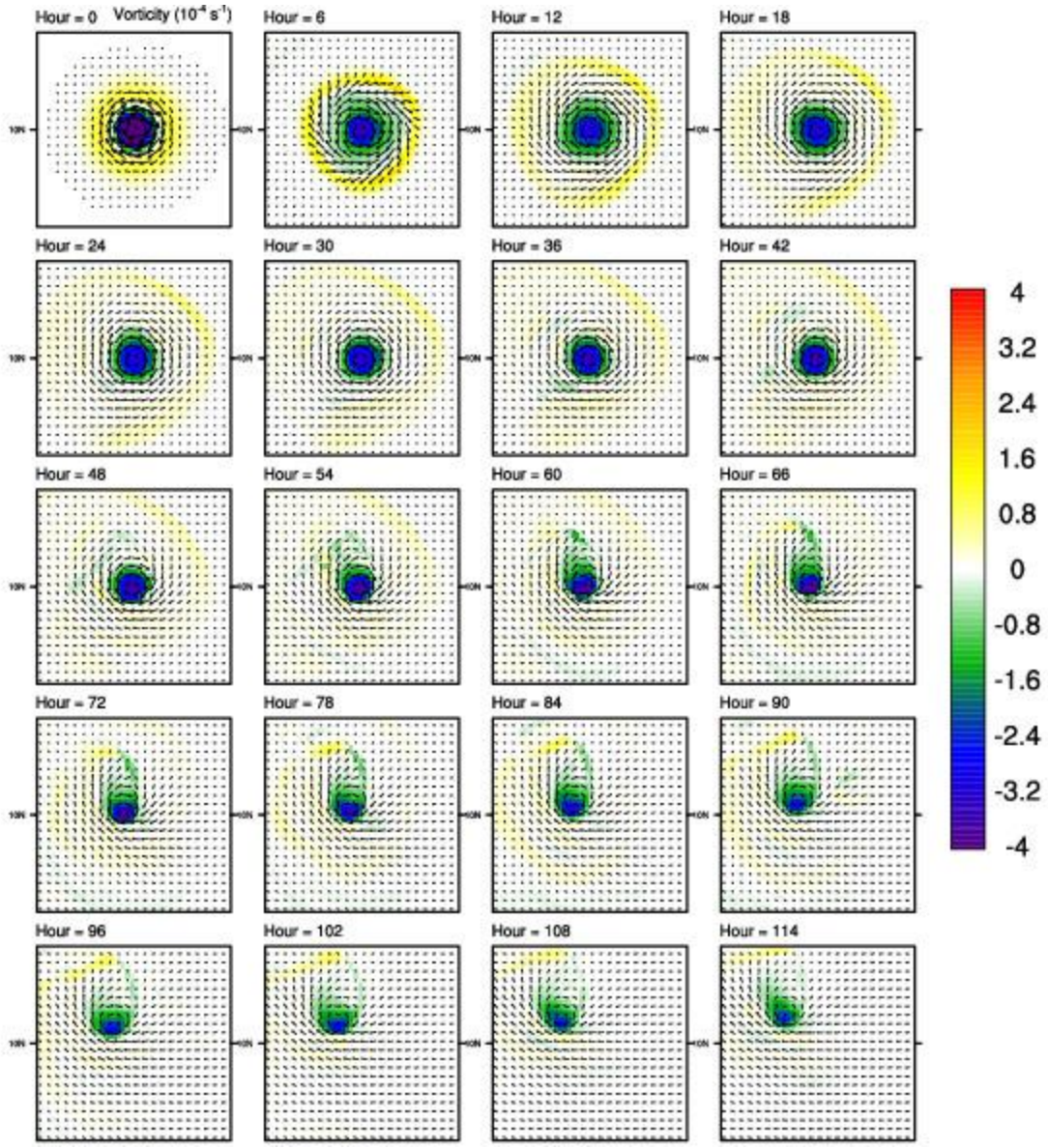

Figure V.4 The vorticity (shading; $*10^{-4}$ s^{-1}) and currents (vectors) averaged from 0 – 15 meters are shown for the NCOM HC simulation. The model simulation hour is shown in the upper left above each panel. Panels are a zoomed in view of the model domain to emphasize features of the eddy.

Next, we examine the behavior of the MLD following the eddy center. The MLD is defined as the depth at which the change in density exceeds 0.125 kg m^{-3} referenced from the surface density. The eddy center is broadly defined as the .09° x .09° box area around the eddy maximum temperature at the surface. The overall results are insensitive to the use of an averaging box. The box area average is used to smooth spurious jumps in the eddy maximum temperature location from one timestep to the next. The eddy-tracking MLDs for the respective simulations are shown in figure V.5.

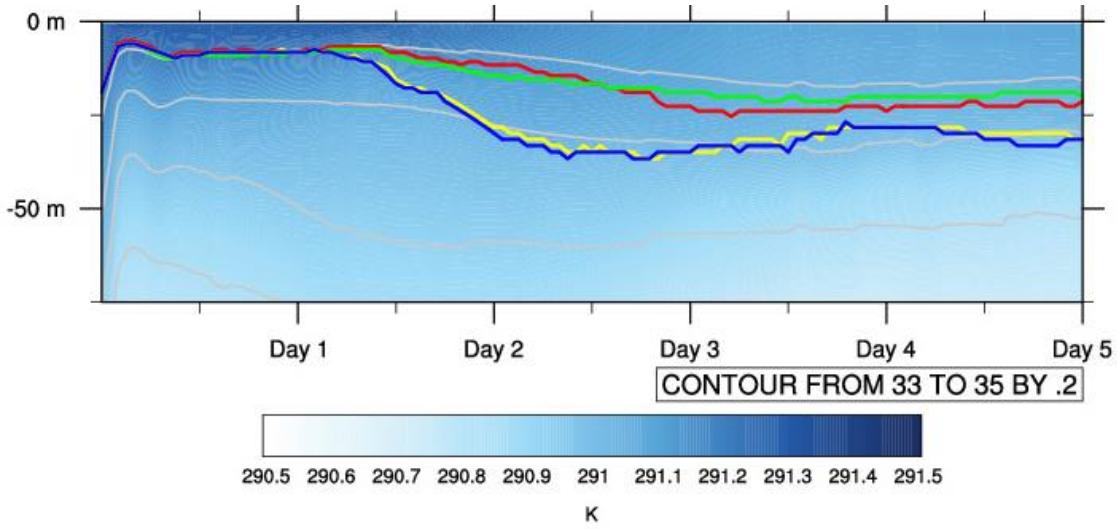

Figure V.5 The temperature (shading; K) and salinity (contours; psu) are shown for the NCOM KC simulation. The respective eddy-tracking MLDs for each simulation are shown in the colored lines (red = HC, green = KC, yellow = MLY, blue = MLY25).

The MLDs following the eddies are consistent among the respective model simulations for the first day, located around 7 – 10 m depths. The MLDs begin to spread near hour 36, the time period when the eddy vorticity structure develops asymmetries in the MLY and MLY25 simulations. The associated weakening of the eddy in the MLY and MLY25 simulations are likely linked to the deepening of the MLD and associated downward transport of momentum such that the eddy surface representation is degraded. The MLD in the KC and HC simulations are shallower than that of MLY and MLY25 following the first day. The HC simulation deepens the MLD more rapidly than the KC simulation during days 2 – 3. The KC and HC simulations both deepen to ~22 m near day 3 and hover around those levels for the remainder of the simulation, suggesting an equilibrium has been reached. However, the MLY and MLY25 simulations deepen to ~30 m at day 2.5 and shoal to ~26 m at day 3.5/day 4, during the period when the eddy weakens rather rapidly and asymmetries in the vorticity field are most notable. Overall, the behavior of the MLD for the MLY and MLY25 simulations changes more quickly and is more oscillatory.

V.II HYCOM Experiments

Two identical HYCOM experiments with an idealized stationary eddy are carried out with a spatially constant wind-stress of 6 $\times 10^{-3}$ Pa (NF) and without surface forcing (ZF). These experiments are repeated for KPP and GISS vertical mixing schemes. The temporal evolution of temperature and density extracted at the eddy center from the simulations are displayed in Figures V.6 and V.7 along with the MLD. The eddy center is identified as the maximum temperature within the eddy. The MLD in the GISS with and without wind-stress forcing is similar (10 – 20 m). For the case with surface forcing (NF), the KPP MLD was 10-20 m. On the contrary, the KPP MLD

without surface forcing deepened to 40 m (Figure V.7). Overall, the GISS MLD was shallower by 10 m than the KPP in all cases except for first 2 days when they were identical. The GISS scheme generate a thicker layer between 30 and 70 m. GISS also exhibits more strongly stratified upper-ocean than the KPP. The different response of mixing schemes to surface forcing can be attributed to the different Ekman buoyancy flux in these vertical mixing schemes.

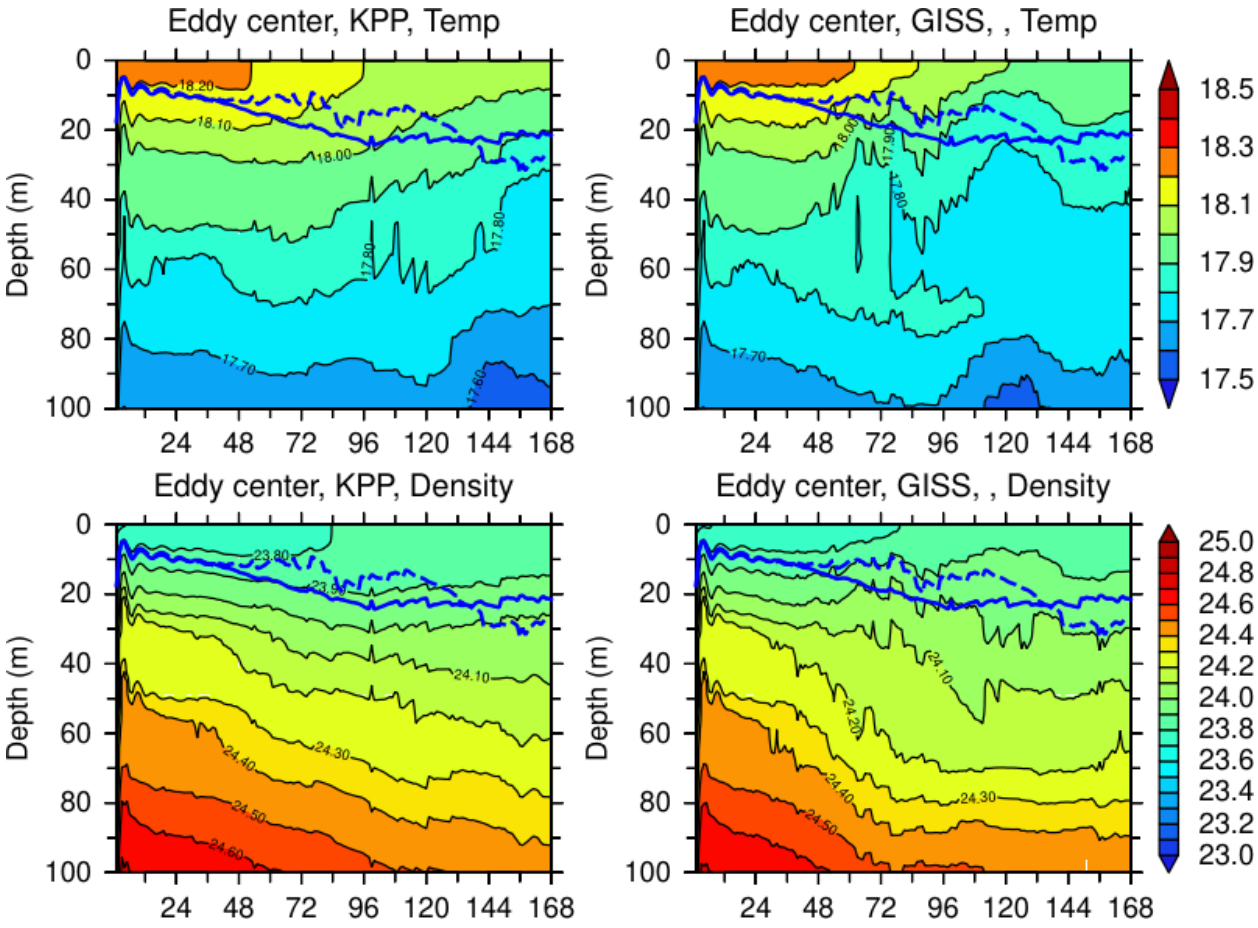

Figure V.6 Time-depth evolution of (top) Temperature (°C) and (bottom) density (kg m^{-3}) from HYCOM simulation using (left) KPP and (right) GISS vertical mixing schemes from the stationary eddy experiment with spatially uniform wind-stress of 6×10^{-3} Pa. The mixed layer depth at the eddy center is plotted for KPP (solid line) and GISS (dashed line). The mixed layer depth is taken as the depth at which the density change equivalent to 0.5°C temperature decrease from the surface. The time in hours on x-axis.

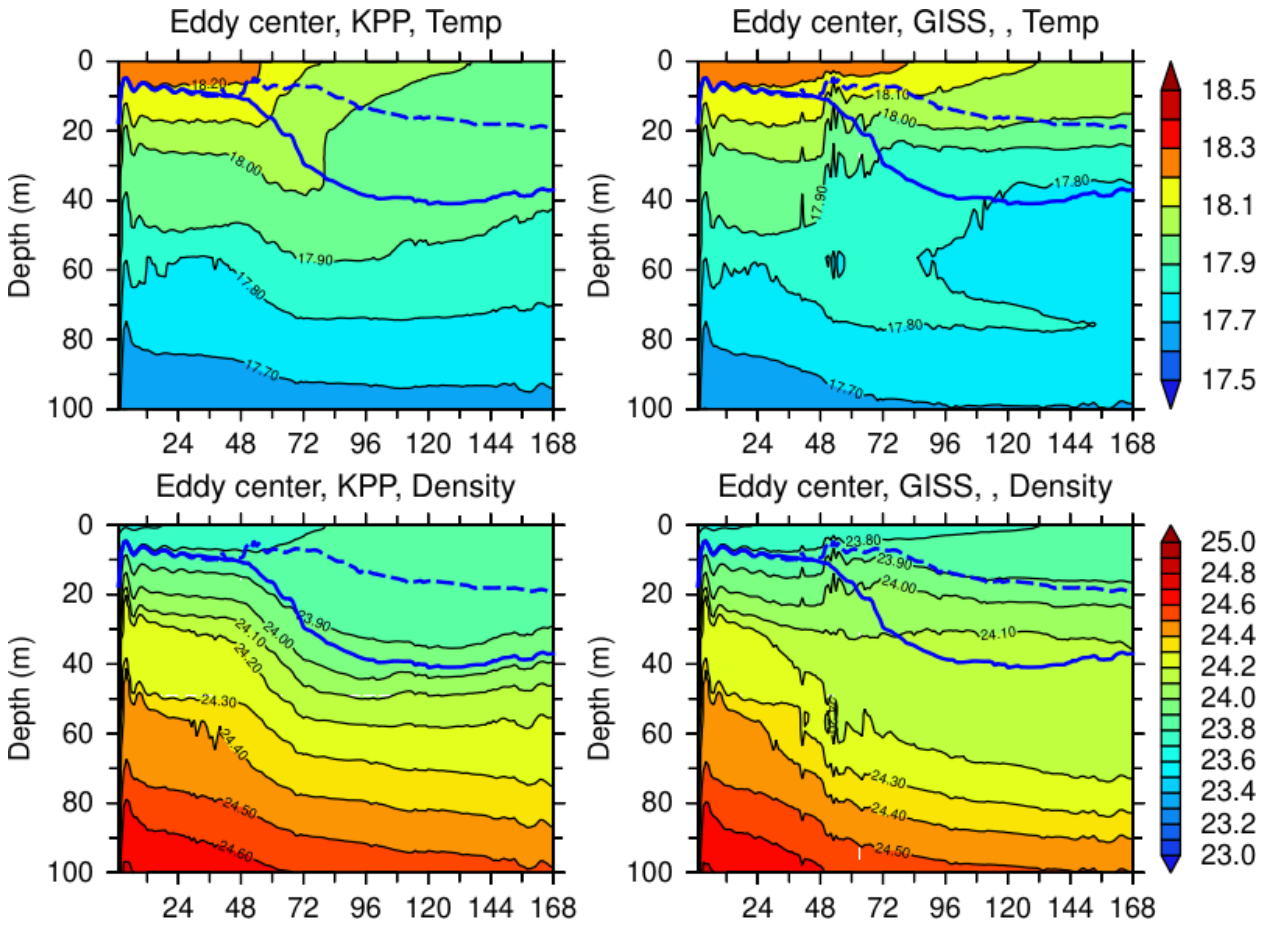

Figure V.7 Time-depth evolution of (top) Temperature (°C) and (bottom) density (kg m^{-3}) from HYCOM simulation using (left) KPP and (right) GISS vertical mixing schemes from the stationary eddy experiment with no surface forcing. The mixed layer depth at the eddy center is plotted for KPP (solid line) and GISS (dashed line). The mixed layer depth is taken as the depth at which the density change equivalent to 0.5°C temperature decrease from the surface. The time in hours on x-axis.

To understand the different response of stationary eddy to the prescribed surface forcing and different vertical mixing schemes, Figures V.8 and V.9 show temporal evolution of surface relative vorticity (10^{-5}, s^{-1}) from hours 48 to 84 centered around the eddy. Noticeable asymmetries in the vorticity field are clear between the KPP and GISS resulting from the deformations in the flow. GISS scheme appears to radiate vorticity away from the eddy center to the north and northwest segment of the eddy which leads to the eddy distortion than KPP (Figures V.8 and V.9, left panels). The different response of the mixing schemes to with and without surface forcing can be attributed to the different Ekman buoyancy flux in these vertical mixing schemes. Without surface forcing, vorticity pattern is more asymmetric in GISS than KPP. This asymmetry in the turbulence field will led to an asymmetric structure of instability around the eddy and thus cause more rapid distortion of the eddy.

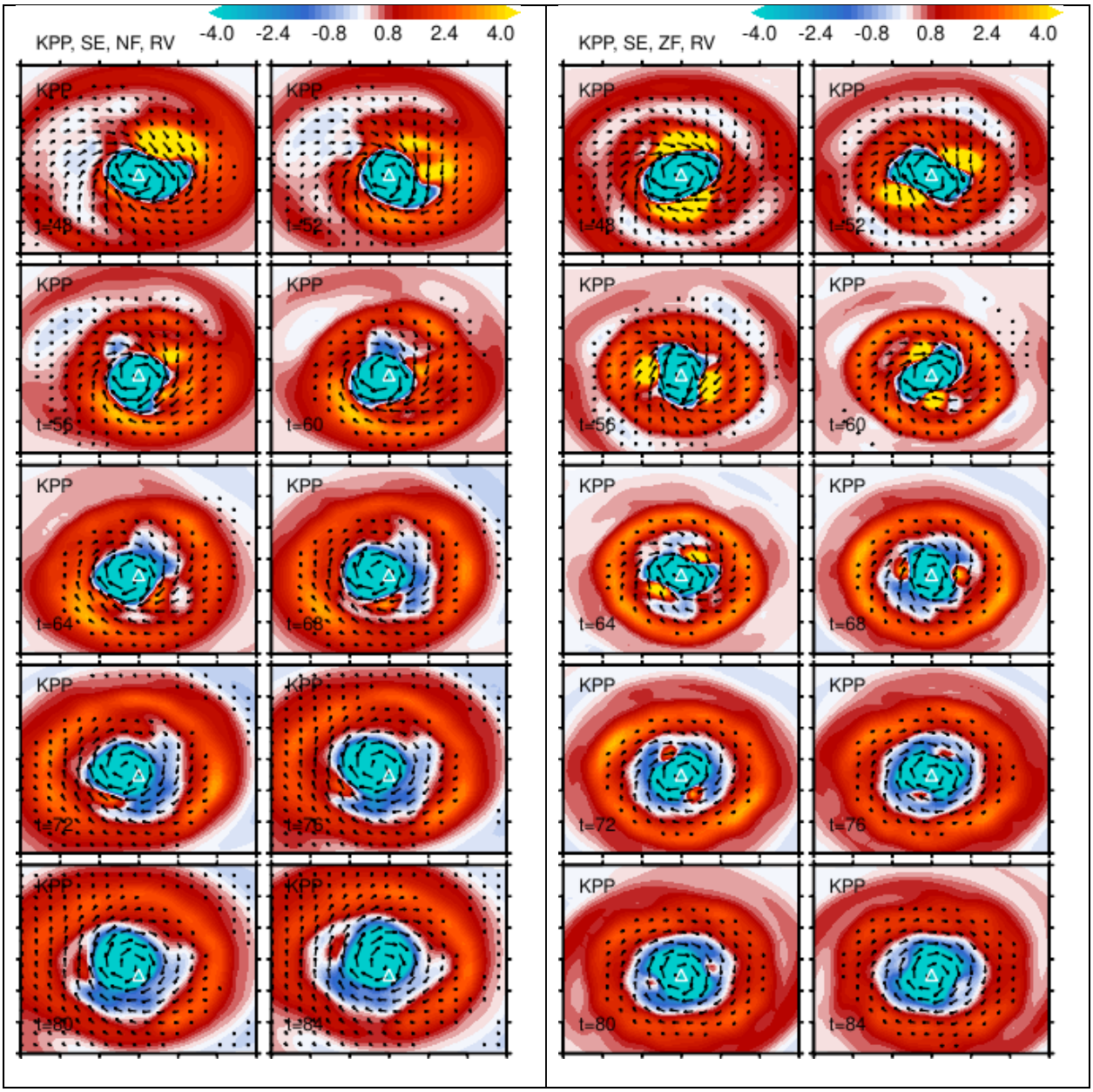

Figure V.8 Time sequences of relative vorticity ($\times 10^{-5}$ s^{-1}) starting 48 through 84 hours from the HYCOM simulations using stationary eddy (left) with spatially uniform surface wind-stress forcing (right) no surface forcing using the KPP mixing scheme.

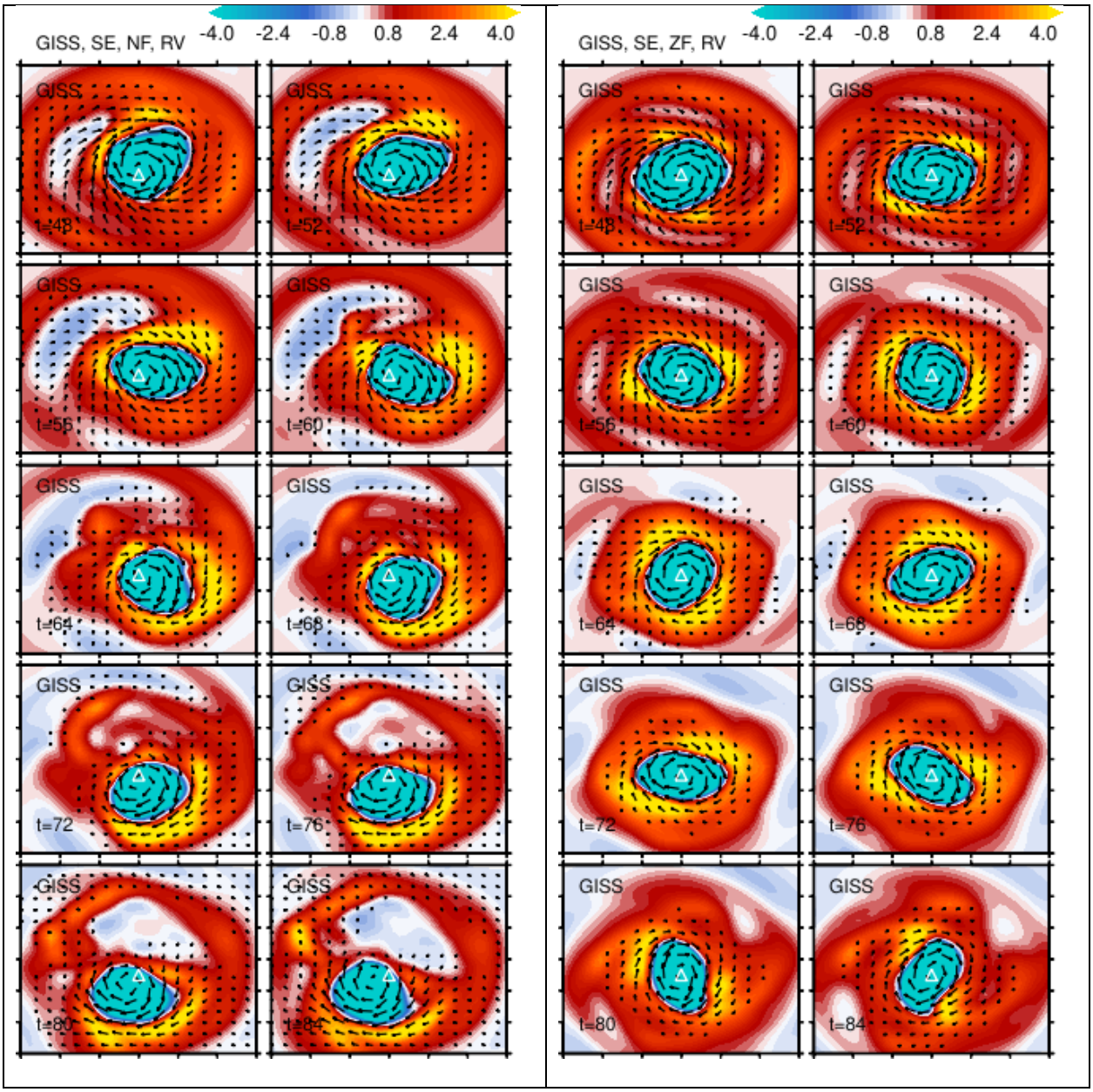

Figure V.9 Time sequences of relative vorticity ($\times 10^{-5}$ s^{-1}) starting from 48 through 84 hours from the HYCOM simulations using stationary eddy (left) with spatially uniform surface wind-stress forcing (right) no surface forcing using the GISS mixing scheme.

VI. Interaction Between Submesoscale Eddies and Ocean Boundary Layer Turbulence

Idealized HYCOM and LES experiments were conducted to understand the effect of submesoscale eddies on boundary layer turbulence.

VI.1 Eddy distortion in the moving case

Eddy distortions in the moving case are analyzed through SST snapshots every 2 hours in the HYCOM simulations (Figures VI.1 – VI.4). We can see, as in the stationary cases, although the eddies are the same at the initial state in the two runs with the GISS and KPP schemes respectively, small magnitude differences start to appear after 6 hours of model simulations. The eddies were able to maintain relatively circular shape during the first 40 hours or so in both simulations and keep its center along the middle cross section of the model domain. Starting from hour 42, the eddy in the simulation with KPP scheme start to show distortion with more stretching in the longitudinal direction and become more oval shaped. The distortion of the eddy started about 10 hours later in the run with the GISS scheme. The shape and magnitude of the eddy become significantly different between the two runs after 60 hours of simulation.

Distortions of the eddy not only present in the horizontal directions, but in the vertical as well. As we can see from the time variation of potential temperature profiles at point C in Figure VI.5, the eddy becomes more contracted in the horizontal with deeper vertical extent in the run with the KPP scheme, while the eddy in the run with the GISS scheme is broader and shallower. Notice that the distortion of the eddy also affected the propagation speed of the eddy. The center of the eddy reaches point C around hour 64 in the run with the KPP scheme, 8 hours ahead of the eddy in the run with the GISS scheme. Due to the large differences in the eddy structure, magnitude, and propagation speed after 60 hours or so in the two simulations, the large-scale gradient forcing produced by these two runs for the LES experiments are too different to be comparable. Thus, we will only compare and analyze the first 64 hours of the HYCOM and LES simulations in the rest of this section since the eddy reaches point C around hour 64 in the run with the KPP scheme. This will give us a complete view of the boundary layer responses when the eddy is away, approaching, and arriving at the locations of our choices.

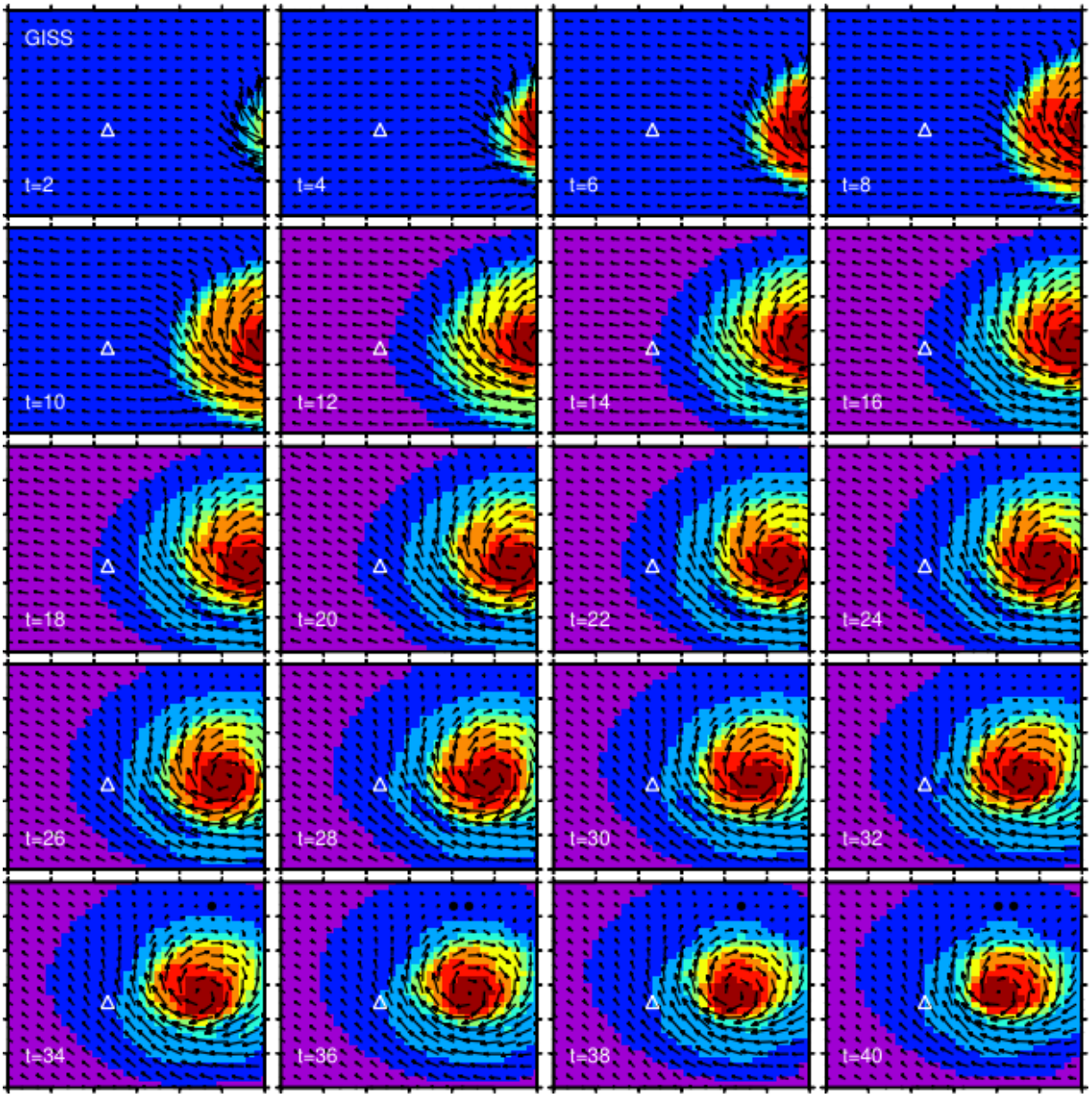

Figure VI.1 Sea surface temperature (SST) at every 2 hour from hour 2 to 40 in the HYCOM run using the GISS mixing scheme. The white triangle in each panel indicates the location of point C.

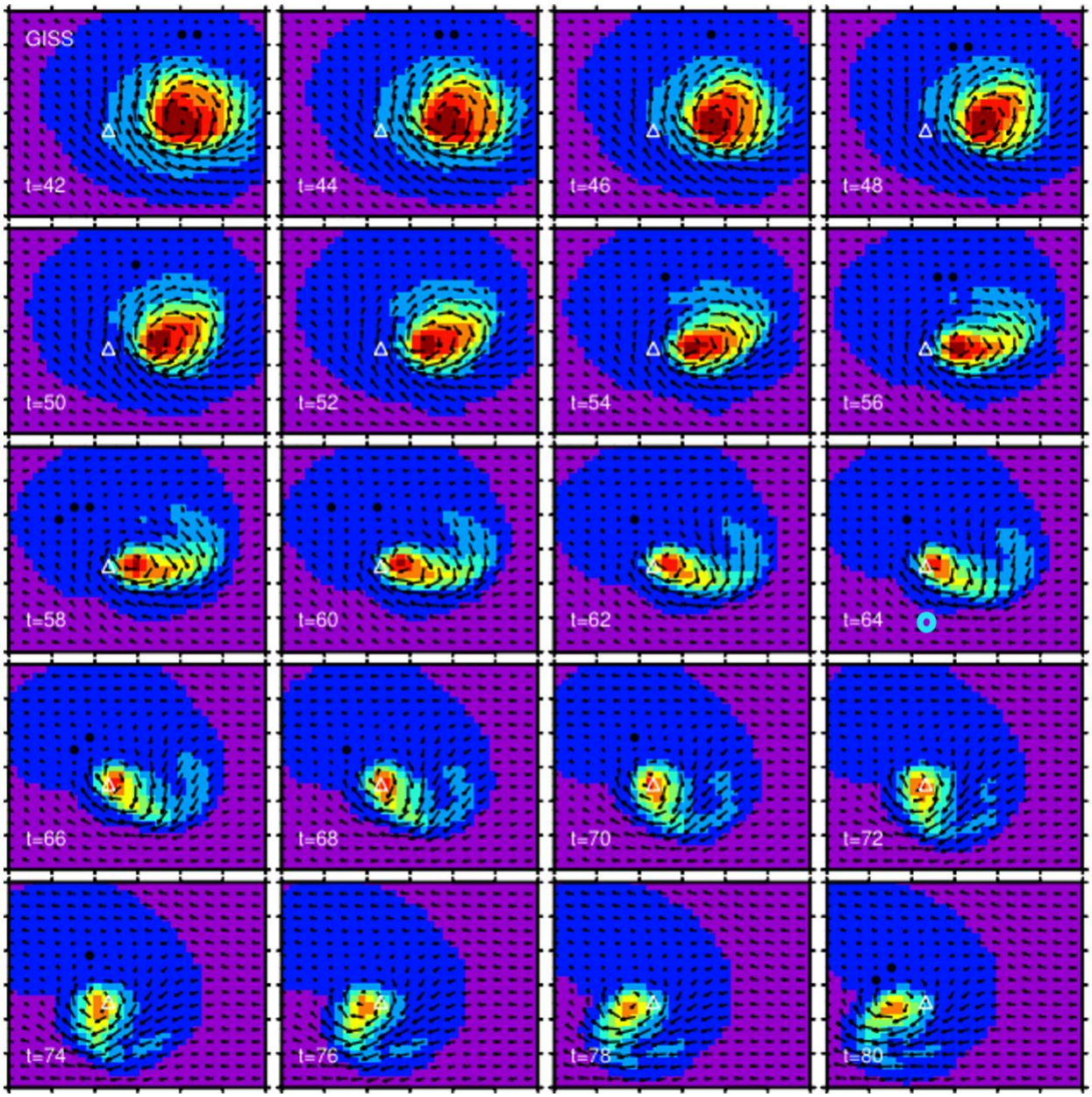

Figure VI.2 Sea surface temperature (SST) at every 2 hour from hour 42 to 80 in the HYCOM run using the GISS mixing scheme. The white triangle in each panel indicates the location of point C. The cyan circle in the hour 64 panel indicates the location of point D.

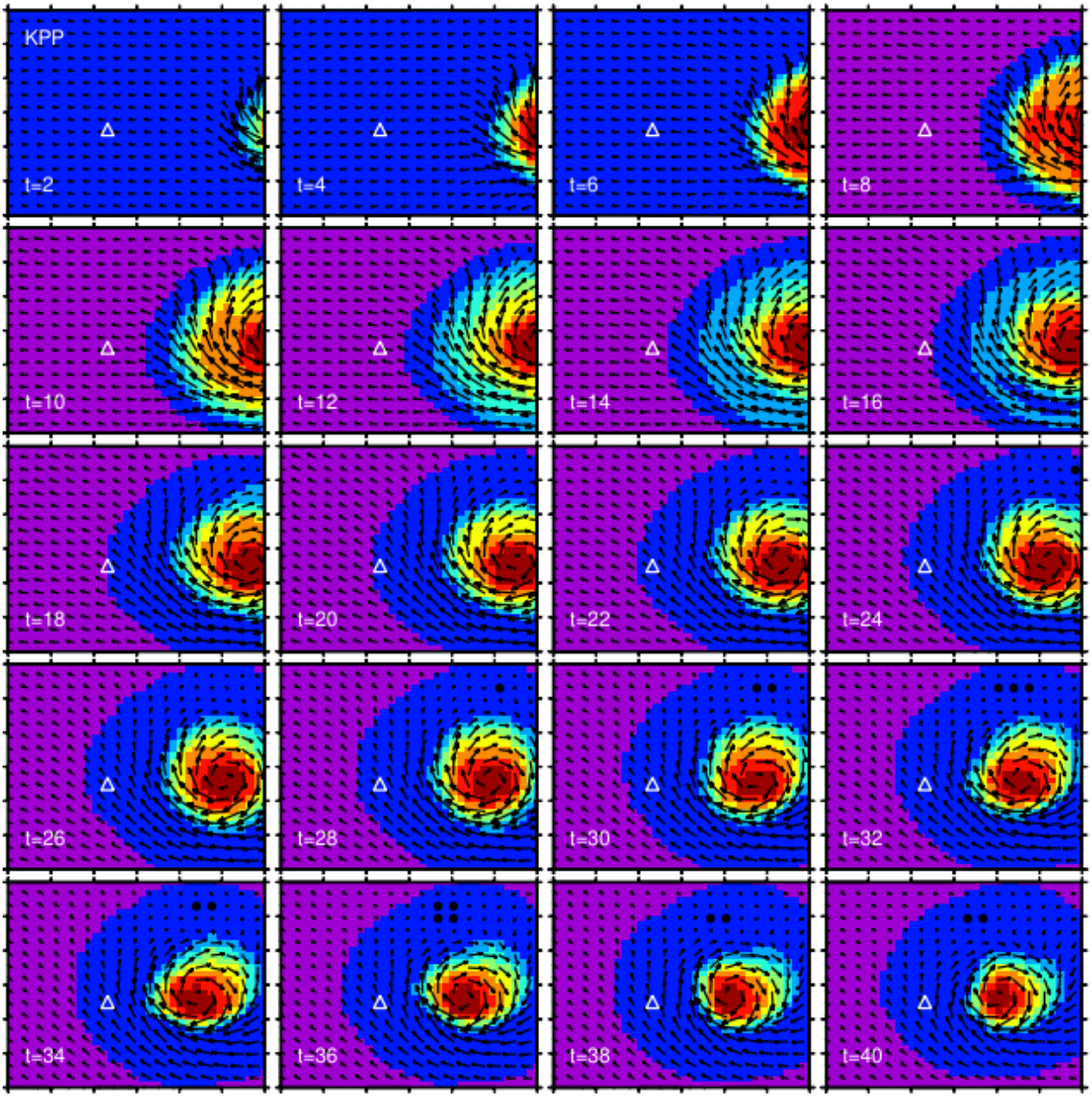

Figure VI.3 Sea surface temperature (SST) at every 2 hour from hour 2 to 40 in the HYCOM run using the KPP mixing scheme. The white triangle in each panel indicates the location of point C.

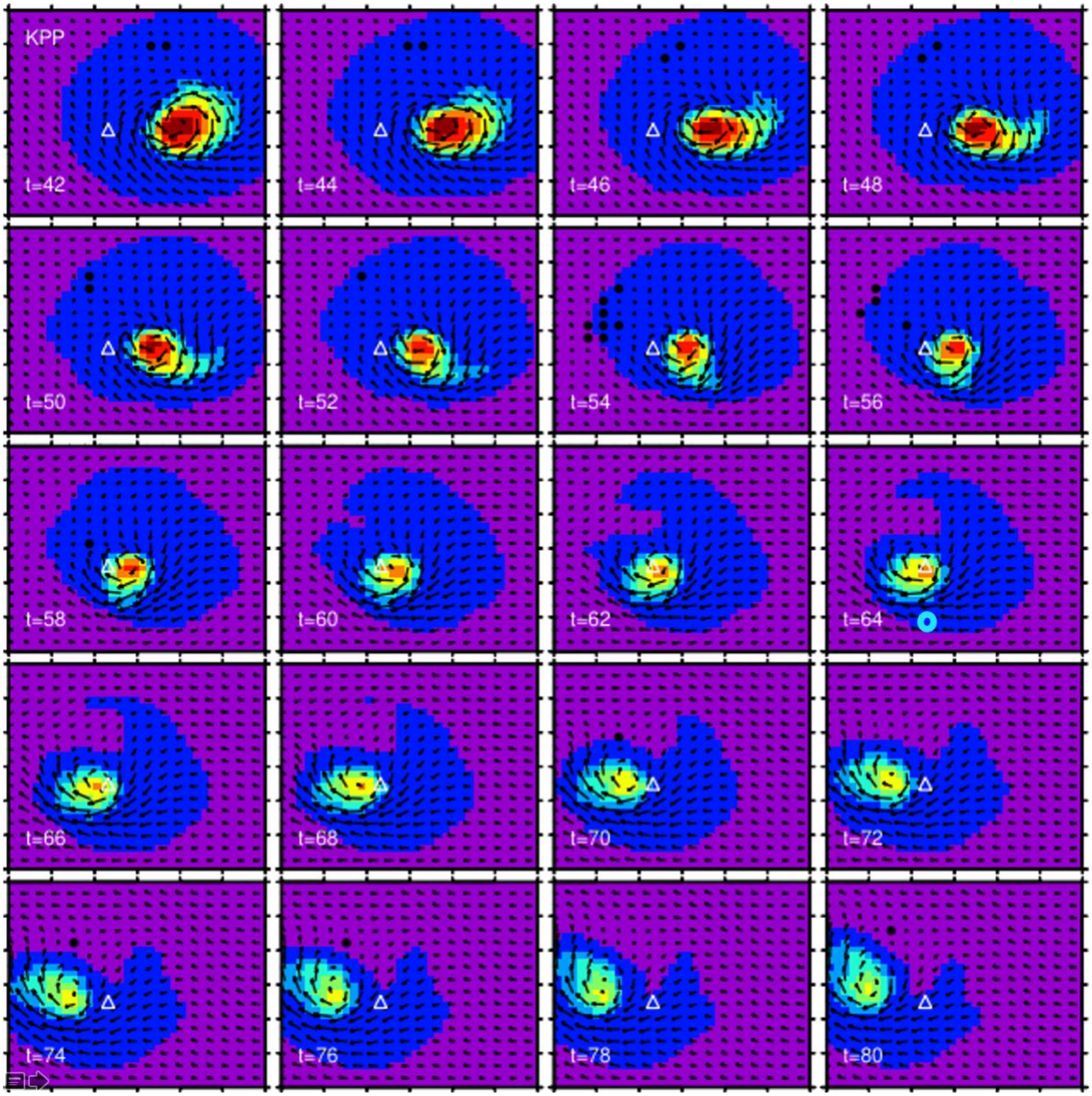

Figure VI.4 Sea surface temperature (SST) at every 2 hour from hour 42 to 80 in the HYCOM run using the KPP mixing scheme. The white triangle in each panel indicates the location of point C. The cyan circle in the hour 64 panel indicates the location of point D.

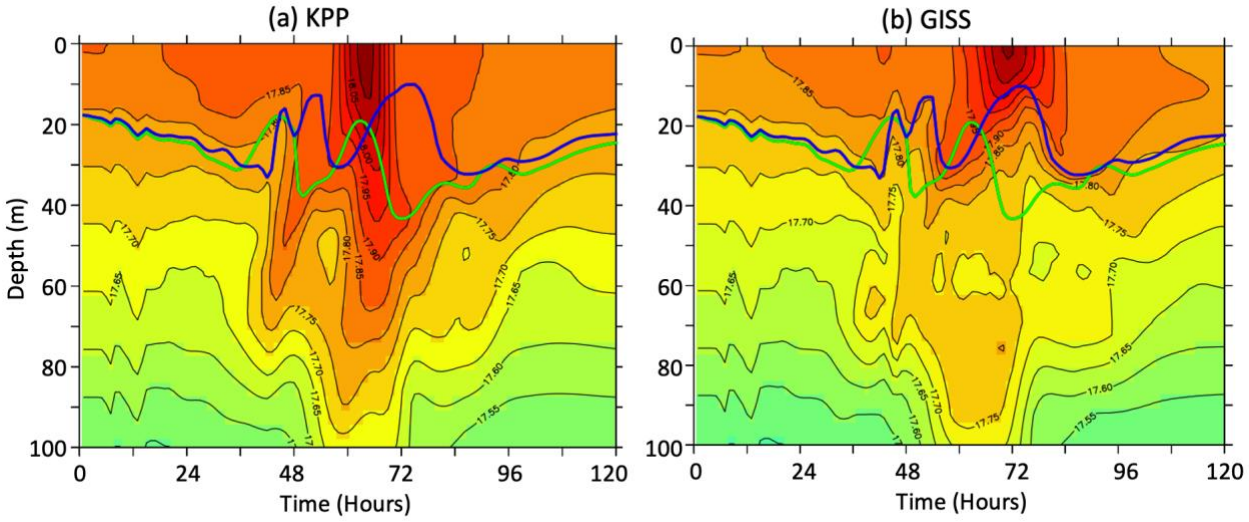

Figure VI.5. Vertical profiles of potential temperature at point C in the HYCOM run with (a) KPP and (b) GISS schemes respectively. The green and blue solid lines in both panels represent the mixed layer depth in the KPP and GISS run respectively. The black thin lines are temperature contours at every 0.5^{o}C.

VI.2 Mixed Layer Dynamics

Mixed layer depth (MLD) is defined as the depth where changes of the potential density referenced to surface are less than 0.1 kg/m^3 for all HYCOM and LES experiments. It is compared at the five chosen locations (Figure VI.6) among the two HYCOM simulations and the LES_GISS and LES_KPP experiments in Figure VI.1. The black and blue lines are MLD from the HYCOM run using the KPP and GISS scheme respectively, the red and cyan lines are MLD from the corresponding LES runs respectively. The distance of the eddy center relative to point C in time in the HYCOM run using the KPP scheme is also given for references. As we can see, the MLD variations are similar between the HYCOM and LES experiments during the first day or so at all five locations. With the approaching of the eddy, the MLD variations become very different at different locations relative to the eddy. Note that since the structure and location of the eddy become significantly different between the HYCOM runs using the KPP and GISS schemes after 64 hours or so of simulations (section VI.1), comparisons among the simulations using different mixing schemes are not performed beyond that time in this study although plots are provided for the entire simulation period of 120 hours.

First, we can see that the LES model produces much stronger deepening than HYCOM on the right-hand side of the eddy (points A and B) for both runs using the KPP and GISS schemes respectively. And this deepening lasted more than a day after the passing of the eddy center. Although there are some differences between the runs using the KPP and GISS schemes (for both HYCOM and LES experiments) due to the different distortions the eddy experienced in the model with these two mixing schemes (see details in section VI.1), the general behavior of the MLD variations among the model runs using two mixing schemes are consistent at point B, and during the first two days at point A. It's curious to notice the sudden deepening of the mixed layer after

the passing of the eddy center in HYCOM run with the KPP mixing scheme. This is most likely caused by the distortion of the eddy.

At point C, while the LES model produces even stronger deepening than the HYCOM simulations before the arrival of the eddy center, the MLD rapidly shallows to 15 m or so when the eddy center arrives, being consistent with the HYCOM model results. The MLD in these two LES simulations are almost identical during the first two and half days or so, then they become significantly different from each other after the arrival of the eddy center. This is due to the very different large scale gradient forcing the two LES experiments receive from the two HYCOM runs that experienced significantly different eddy distortions after 60 hours or so.

On the left hand side of the eddy, however, the LES model produced much shallower MLD than HYCOM at point D and similar MLD to HYCOM at point E. Also notice that the significant difference between HYCOM KPP and GISS simulation at point D after the arrival of the eddy center. This again, as point A, is due to the different distortions the eddy experienced in these two HYCOM runs. The eddy structures become very different between these two simulations after 50 to 60 hours (Figure VI.2 and VI.4). The eddy in the GISS run is more elongated, while the eddy in the KPP run tends to be more circular. For example, the white triangle and cyan circle at hour 64 on these panels indicate the location of point C and D. You can see that point C is right at the center of the eddy for the KPP run, while the eddy center in the GISS run reached the point C at a later time. The eddy propagation was slightly slower in the GISS run relative to the KPP run due to the different distortions the eddy experienced as we discussed in section VI.1. Thus, the vertical structure of the temperature, salinity and currents at point D are very different between these two runs and hence lead to different behavior in the mixed layer responses in these two simulations.

In the following sessions, we will analyze the stratification and turbulence at point B, C, and D to try to understand what has caused the different behavior between the HYCOM and LES simulations. We will only focus on the HYCOM experiment using the KPP scheme in this report. The KPP is an advanced surface boundary layer approximation with simple parameterizations to represent a range of mixing processes in the ocean interior. It is a non-local, mean-field closure model since the estimates of the vertical mixing coefficients made by the KPP scheme are based on the surface boundary forcing and the state of the resolved velocity and potential density fields in the water column, which makes it quite different from other commonly used boundary-layer models, such as the SMTC models.

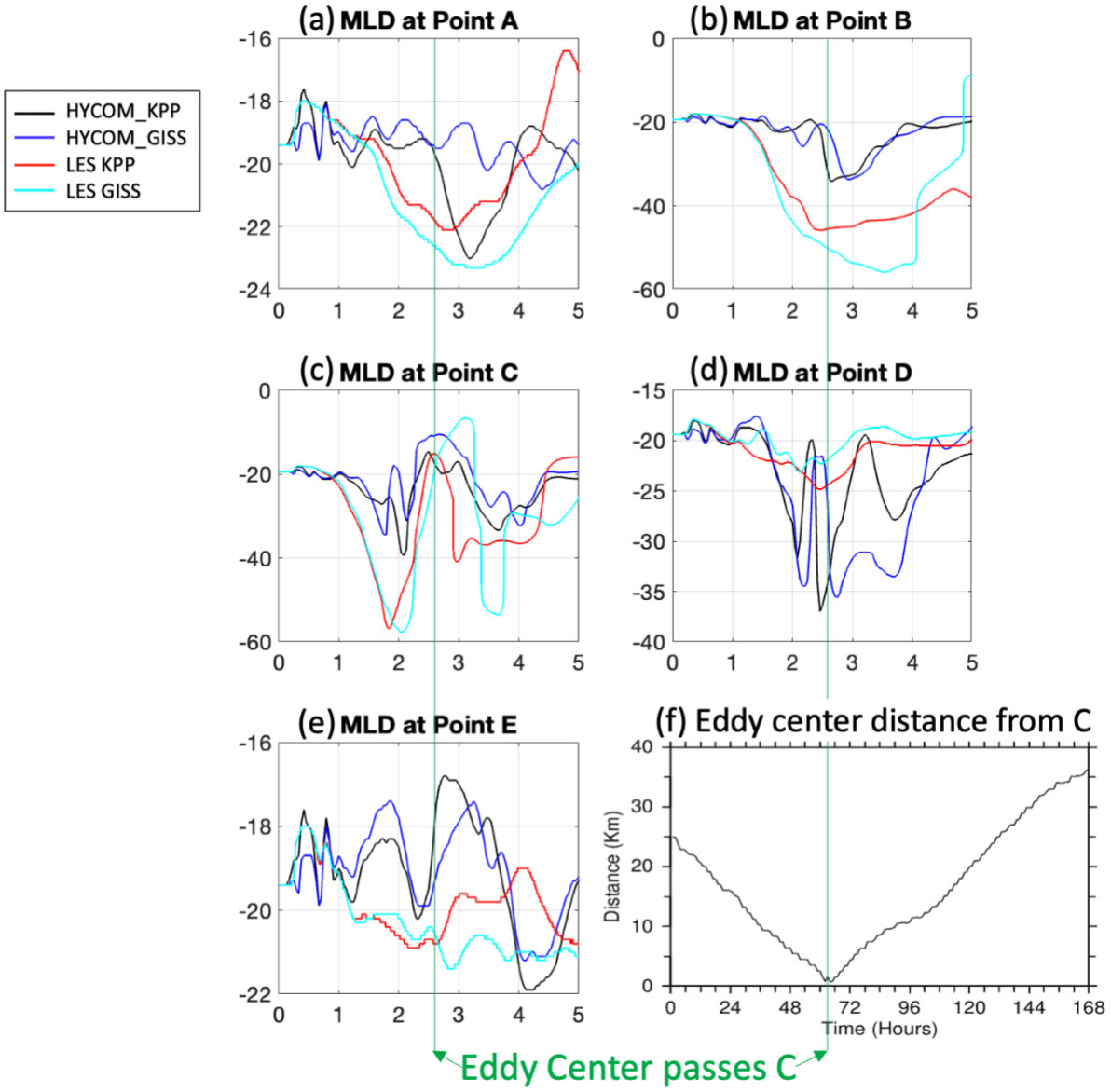

Figure VI.6 Mixed layer depth (MLD) comparison at Points (a) A, (b) B, (c) C, (d) D, and (e) E among HYCOM experiments using the KPP (black) and GISS (blue) schemes, and LES experiments that is forced by HYCOM run using the KPP scheme (red) and GISS scheme (cyan). (f) Distance of the eddy center from point C in km in the HYCOM run using the KPP scheme. The green lines highlight the time when the eddy center passes point C.

a. Along the center of the Eddy

The mixed layer behavior along the center of the eddy will be analyzed at point C in this section. Time variation of potential density profiles from the HYCOM and LES simulations are compared in Figure VI.7 between hour 12 and 66 when the MLD shows significant differences between the two simulations. To better understand the reason for the discrepancy, we also compare the eddy

viscosity (K_m) in these two experiments. The eddy viscosity is parameterized using the KPP scheme in HYCOM and directly outputted from the simulation. The eddy viscosity from the LES simulation is calculated using the Reynolds stress and mean shear following McWilliams et al. (2012):

$$K_{m\_les} = \frac{|\langle \boldsymbol{u}'w \rangle|}{|\partial_z \langle \boldsymbol{u}^L \rangle|} \tag{25}$$

Here, $\langle \boldsymbol{u}'w \rangle$ is the horizontal domain averaged total Reynold stress, and $<\boldsymbol{u}^L>$ is the horizontal domain averaged Lagrangian velocity.

Three time instances were highlighted on the figure with the dashed white lines for hour 24, 34, and 48 that marked three different stages of the eddy location relative to point C (Figure VI.8). The eddy reaches point C at hour 34, before that, the eddy seems to have no effect at point C in the HYCOM simulation, and the mixed layer gradually deepens due to the surface forcing as we can see here from the eddy viscosity (Figure VI.7a and b). After the arrival of the eddy at hour 34, the turbulence in the water column gradually increases due to the enhanced vertical shear brought by the eddy field (Figure VI.7b). Around hour 48, when the eddy center is about 5 km away from C, the vertical shear associated with the eddy becomes stronger and thus leads to large increase of turbulent mixing and sharp deepening of the mixed layer. The mixed layer then rapidly shallows shortly after as the eddy center approaches C, and stratification in the water column is dominated by the eddy structure at the arrival of the eddy center.

The mixed layer responds to the eddy very differently in the LES model. Unlike HYCOM, the LES mixed layer started rapid deepening shortly after hour 24, and before the arrival of the eddy (Figure VI.7c). We can see the enhanced mixing at point C due to the horizontal gradient of temperature, salinity, and current brought by the eddy (Figure VI.7d). Notice, the magnitude of the color-bar for K_m is 15 times larger than that in the HYCOM simulation. That is why we don't see the mixing in the surface layer anymore, because they are too small compared to the strong mixing we see in the mixed layer. When the eddy reaches point C, the turbulent mixing dramatically increases and leads to a rapid mixed layer deepening to almost 60 m. As the center of the eddy approaches C, the mixing weakens, and the mixed layer shallows correspondingly, and reduces to about 15 m when the eddy center arrives and dominates the vertical stratification in the water column.

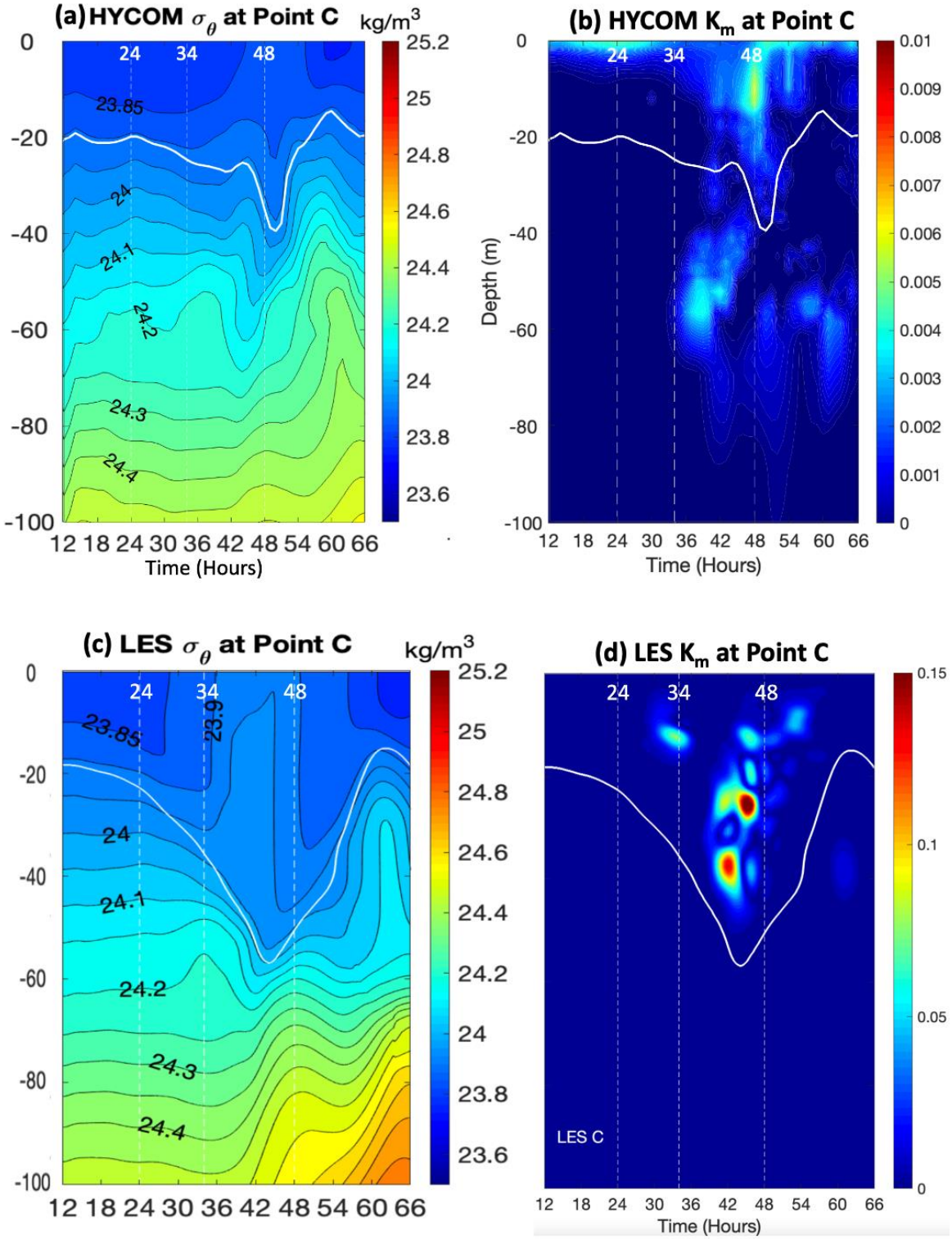

Figure VI.7 Potential density (σ_θ) and eddy viscosity (K_m) at Point C in the HYCOM simulation with KPP scheme and LES experiment LES_KPP1. The white solid line is the MLD in the experiment, and the white dashed lines indicate simulation hour 24, 34 and 48 respectively as marked.

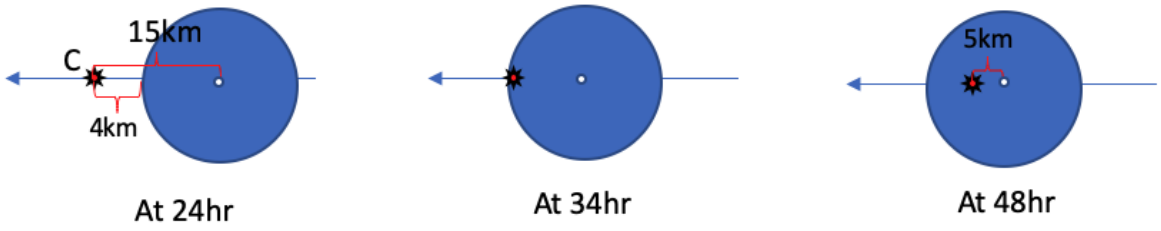

Figure VI.8 Eddy location relative to point C at simulation hour 24, 34, and 48.

If we look at the MLD and turbulence structure between these two simulations, the major difference between them is from hour ~24 to ~48, when the LES shows strong enhanced turbulent mixing and rapid deepening of the mixed layer. To better understand the reason for this, we next analyze the horizontal domain averaged turbulent kinetic energy (TKE) budget in the LES simulations as given in equation (26) below:

$$\frac{\partial e}{\partial t} = TurT + ShearP + BuoyP + PrsT + StokesP - \varepsilon + sgs \qquad (26)$$

where,

$TurT = -\frac{1}{2}\left(\frac{\partial\langle u'^2 w'\rangle}{\partial z} + \frac{\partial\langle v'^2 w'\rangle}{\partial z} + \frac{\partial\langle w'^2 w'\rangle}{\partial z}\right)$ is the turbulent transport term,

$ShearP = -\langle u'w'\rangle \cdot \frac{\partial\langle u\rangle}{\partial z} - \langle v'w'\rangle \cdot \frac{\partial\langle v\rangle}{\partial z}$ is the shear production term,

$BuoyP = \alpha g\langle\theta' w'\rangle - \beta g\langle s' w'\rangle$ is the buoyancy production term,

$PrsT = -\frac{1}{\rho_0}\frac{\partial\langle p' w\rangle}{\partial z}$ is the pressure transport term,

$StokesP = -\langle u'w'\rangle\frac{\partial u_{sx}}{\partial z} - \langle v'w'\rangle\frac{\partial u_{sy}}{\partial z}$ is the Stokes production term,

e is the total TKE, ε is the kinetic energy dissipation rate, and sgs is the subgrid-scale contribution. The angle bracket in the above equations represents horizontal domain average, the superscript prime denotes a departure from the mean value.

The terms in the TKE budget normalized by $u_*^2 f$ are presented in Figure VI.9. They show strong TKE and dissipation associated with the rapid deepening. As the edge of the eddy approaches point C, the strong horizontal shear in T, S, and currents leads to enhanced shear production shortly after hour 24. Then the shear production diminishes when the eddy continues moving westward and point C reaches the periphery of the eddy where we have minimum horizontal gradients in the region. After ~10 hours, with the eddy propagating farther west, the region of the eddy with strong horizontal gradients reaches point C and induced strong turbulent velocity fluctuations that further act on the mean vertical shear and enhanced the TKE. This leads to even stronger shear production and deepening of the mixed layer. Strong turbulent transport and

pressure transport are also observed associated with the enhanced shear production to redistribute the enhanced turbulent energy throughout the water column.

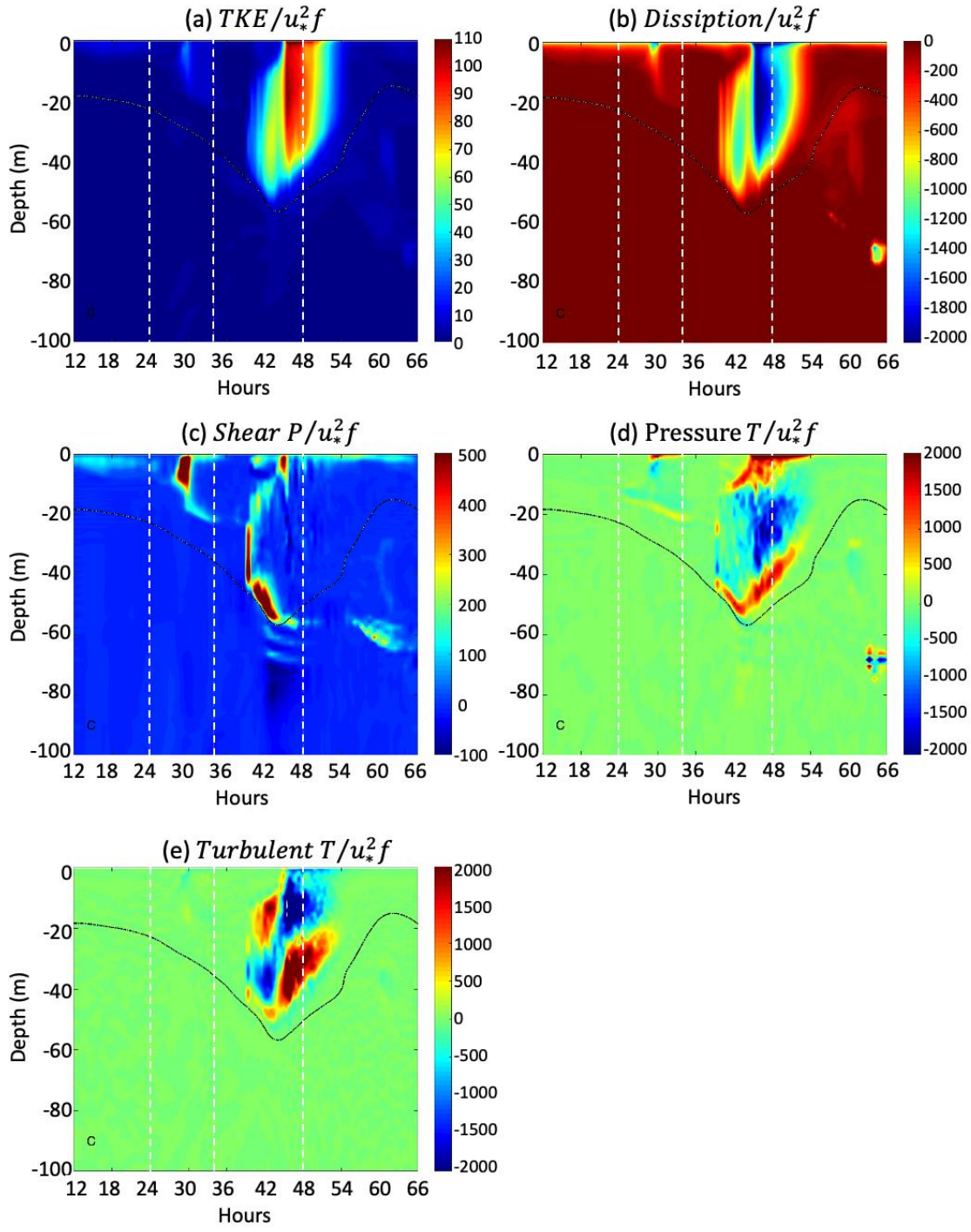

Figure VI.9. Normalized (a) TKE (e), (b) dissipation (ε), (c) shear production (ShearP), (d) pressure transport (PrsT), and (e) turbulent transport (TurT) at point C in simulation LES_KPP1. The black line is the MLD in the experiment, and the white dashed lines indicate simulation hour 24, 34 and 48 respectively as marked.

The absence of enhanced mixing in HYCOM results from the KPP parameterization. Its mixing coefficient is a function of the surface boundary forcing and the state of the resolved velocity and potential density fields instantaneously in the water column. This means that the KPP parameterization is insensitive to the horizontal gradients, which, as demonstrated by the LES simulations, are the main source of turbulent mixing as the eddy approaches point C.

b. On the Right-Hand Side of the Eddy

The mixed layer behavior on the right-hand side of the eddy will be analyzed at point B in this section. Time variation of potential density and eddy viscosity profiles from the HYCOM and LES simulations are compared in Figure VI.10 between hour 12 and 66. The stratification and MLD variation in the water column are very similar between these two models during the first 36 hours or so. Significant differences between the two simulations are observed after that when rapid mixed layer deepening is observed in the LES experiment, while there are not much changes in the mixed layer for the HYCOM experiment until around hour 60 when a sudden deepening occurred.

Since we have a warm core eddy with a cyclonic current, as the eddy approaching point B, after hour 36, the wind direction is either aligned or within a small angle to the geostrophic current associated with the eddy. In the LES simulation, the Ekman transport generated by the wind forcing transports the water southward and thus brings denser water over less dense water, which will result in a convectively unstable state and destabilize the water column. The resulting wind-driven advective buoyancy flux divergence is sometimes characterized as an effective surface or Ekman buoyancy flux (Thomas and Lee 2005; Thomas and Taylor 2010). This will lead to enhanced turbulence and deepening of the mixed layer (Skyllingstad 2017) as evidenced in the enhanced eddy viscosity (Figure VI.10d), TKE (Figure VI.11a) and vertical velocity (Figure VI.11f).

While the Ekman buoyancy flux may, for destabilizing winds, contribute to TKE generation through mechanically forced convection, the presence of geostrophic shear that is aligned with the wind-driven shear can also augment the wind-driven TKE generation. This occurs through mechanical shear production, in which wind-driven turbulent velocity fluctuations further act on the mean vertical shear and enhance the TKE (Figure VI.11c). We also see strong turbulent transport and pressure transport associated with the enhanced shear production to redistribute the enhanced turbulent energy throughout the water column as observed at point C.

However, these processes are not well represented by KPP in the HYCOM simulation. There are barely any changes in the mixed layer until around hour 60 when a sudden deepening occurred. This is caused by the enhanced turbulent mixing in the water column due to the strong vertical shear brought by the eddy as its center gets closer to point B.

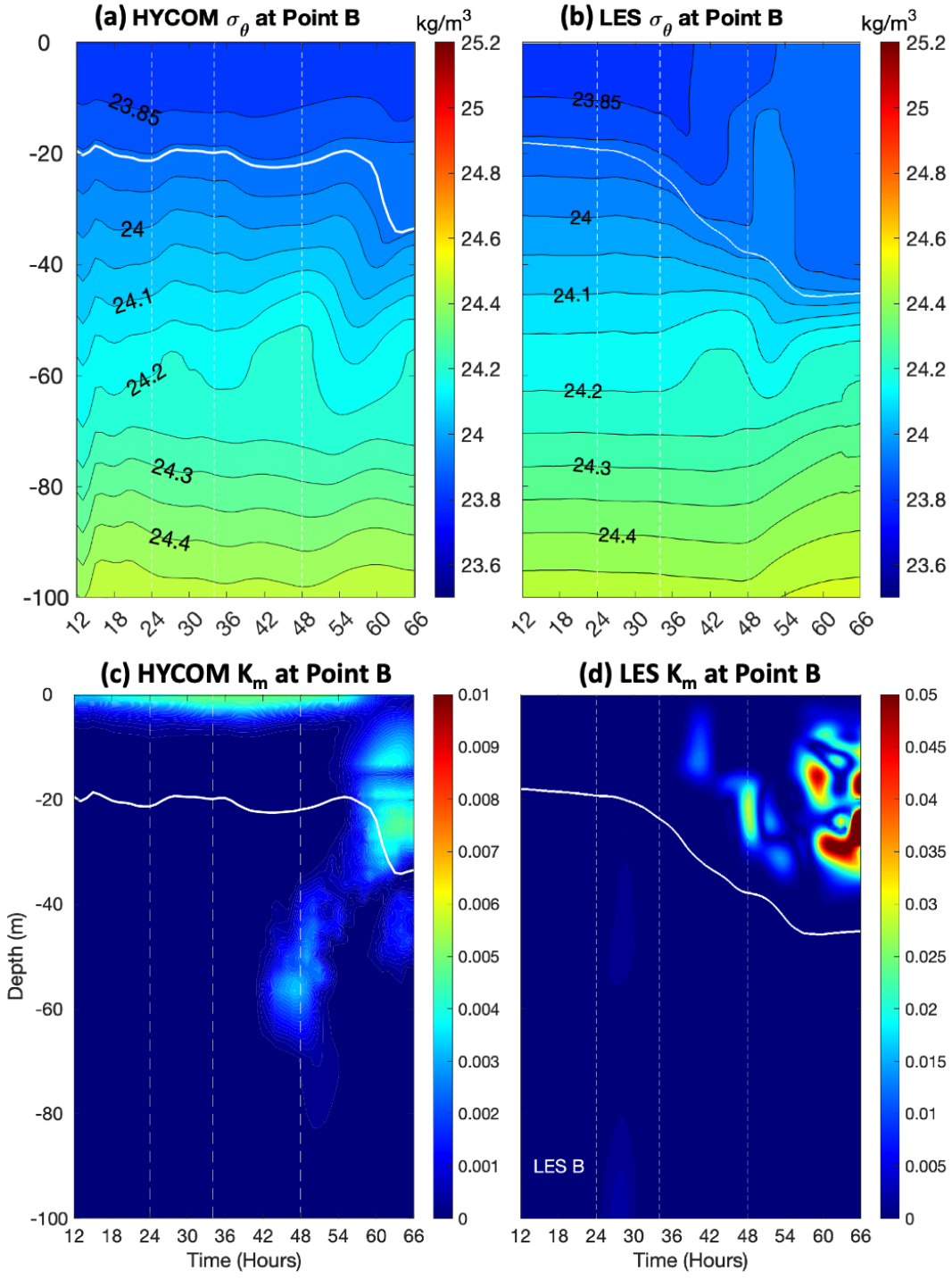

Figure VI.10 Potential density (σ_θ) and eddy viscosity (K_m) at Point B in the HYCOM simulation with KPP scheme and LES experiment LES_KPP1. The white solid line is the MLD in the experiment, and the white dashed lines indicate simulation hour 24, 34 and 48 respectively as marked.

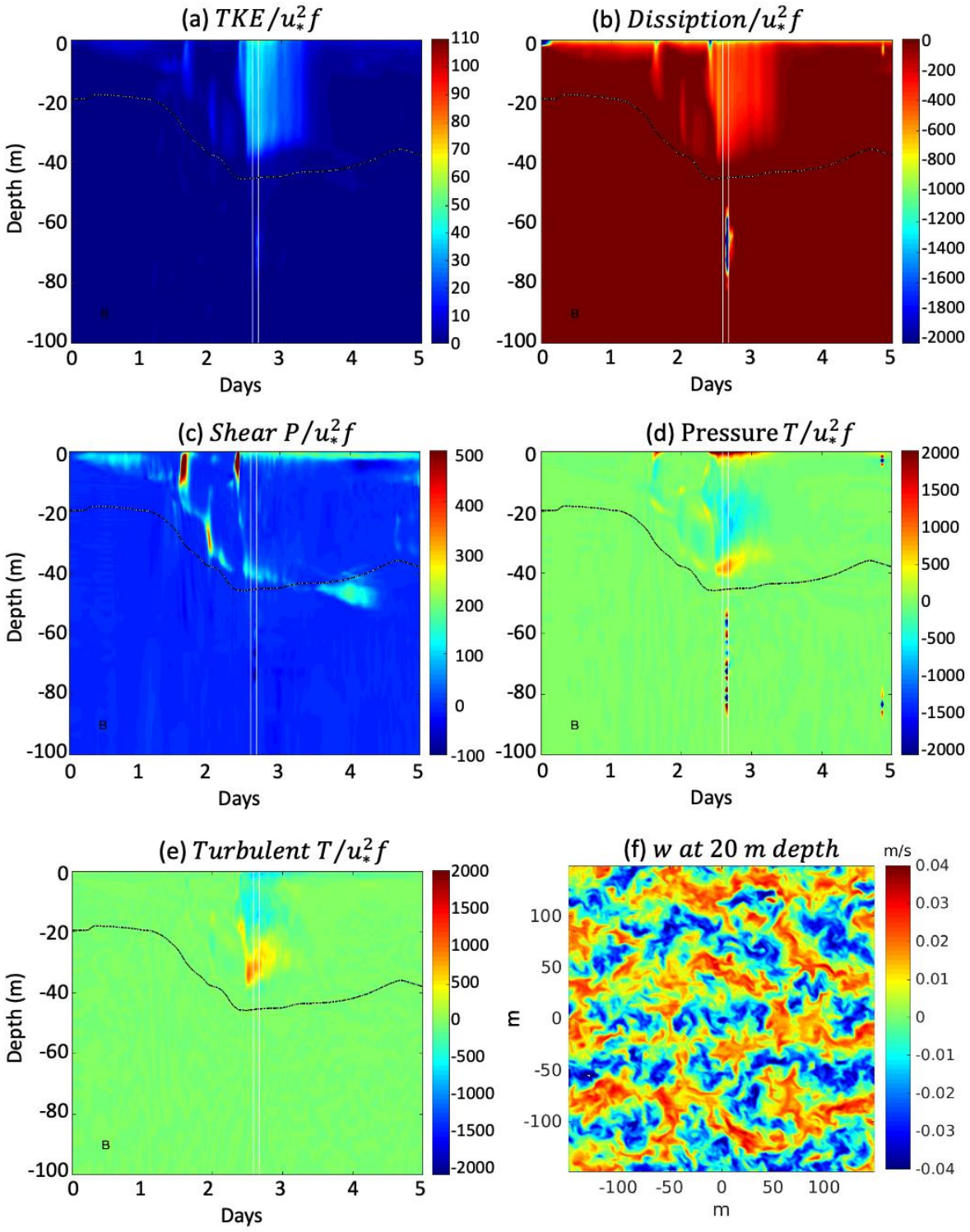

Figure VI.11. Normalized (a) TKE (e), (b) dissipation (ε), (c) shear production (ShearP), (d) pressure transport (PrsT), and (e) turbulent transport (TurT) at point B in simulation LES_KPP1. The black line is the MLD in the experiment, and the white lines highlights the period when the center of the eddy passes the middle cross-section of the model domain. (f) Instant vertical velocity w at 20 m depth after 60 hours of model simulation.

c. On the Left-Hand Side of the Eddy

The mixed layer behavior on the left-hand side of the eddy will be analyzed at point D in this section. Time variation of potential density and eddy viscosity profiles from the HYCOM and LES simulations are compared in Figure VI.12 between hour 12 and 66. The MLD variation in the water column are very similar between these two models during the first 34 to 36 hours. Significant differences between the two simulations starts afterwards when a rapid deepening up was observed in the HYCOM simulation while there is almost no mixed layer deepening in the LES experiment.

Notice that the mixed layer depth at point D is a little deeper than that at point B in the HYCOM simulation. This is because, due to the eddy distortion, the currents associated with the eddy are stronger at point D than B (Figure VI.4) and thus results in stronger shear productions and mixing.

Opposite to point B, at point D, winds are aligned with the front such that denser water is to the right of the wind direction, then Ekman current shear is stabilizing, as it transports lighter water over dense water and leads to stable stratification and shallowing of the mixed layer. We can see the surface lighter fluid intrusion in the LES simulation due to this effect in Figure VI.12b. Since the Ekman buoyancy flux is not represented in the HYCOM simulations and thus its density plot shows no surface lighter fluid intrusion (Figure VI.12a). The stabilizing effect of Ekman buoyancy flux on turbulence can be observed from the LES simulation as well. The TKE and shear production are very weak at point D and cannot penetrate through the entire depth of the mixed layer (Figure VI.13). Although we see stronger eddy viscosity in the LES simulation than HYCOM (Figure VI.12), it is only confined within the middle of the mixed layer, and thus can only work to mix the water within the mixed layer but is not able to deepen the mixed layer.

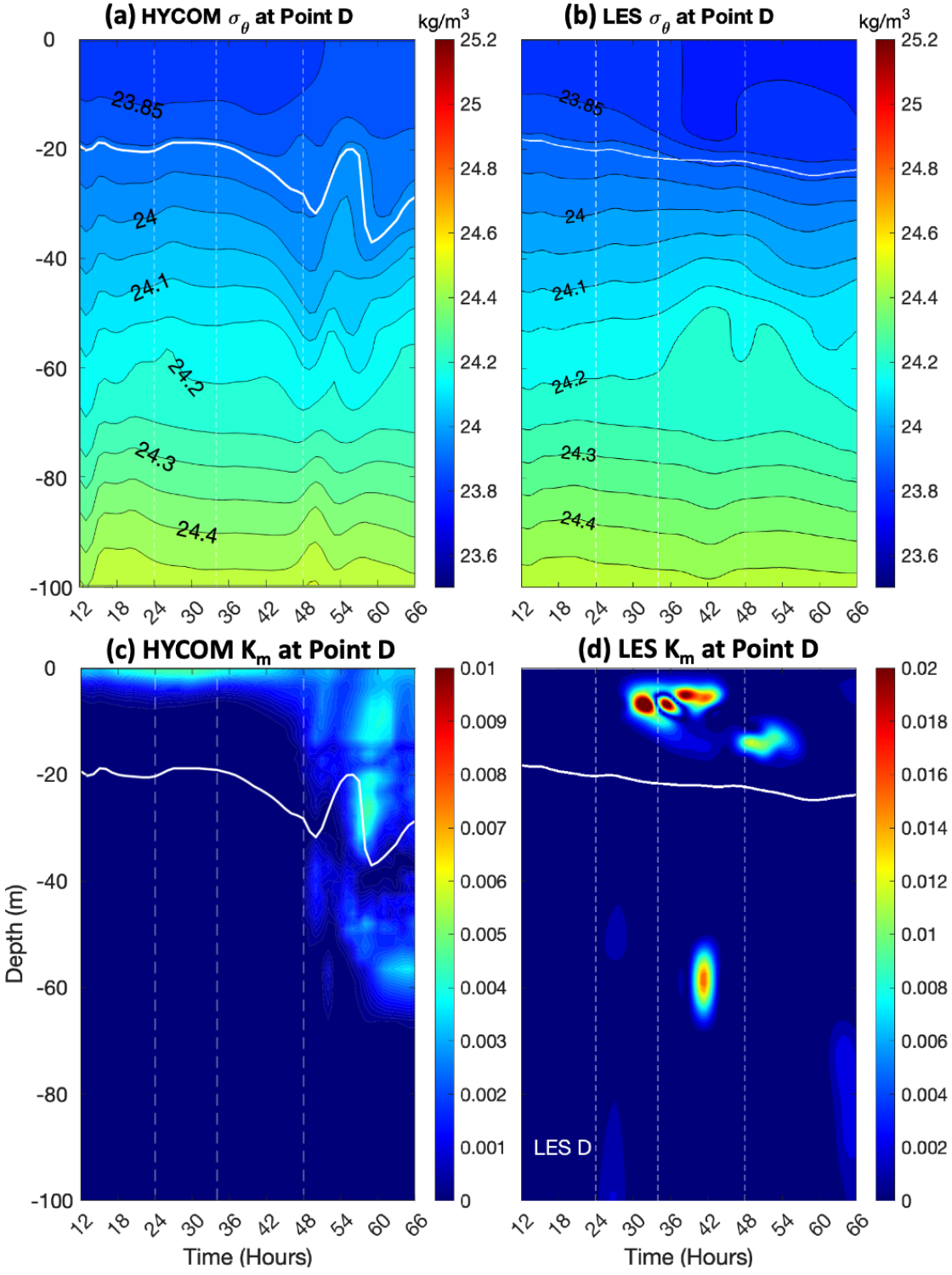

Figure VI.12 Potential density (σ_θ) and eddy viscosity (K_m) at Point D in the HYCOM simulation with KPP scheme and LES experiment LES_KPP1. The white solid line is the MLD in the experiment, and the white dashed lines indicate simulation hour 24, 34 and 48 respectively as marked.

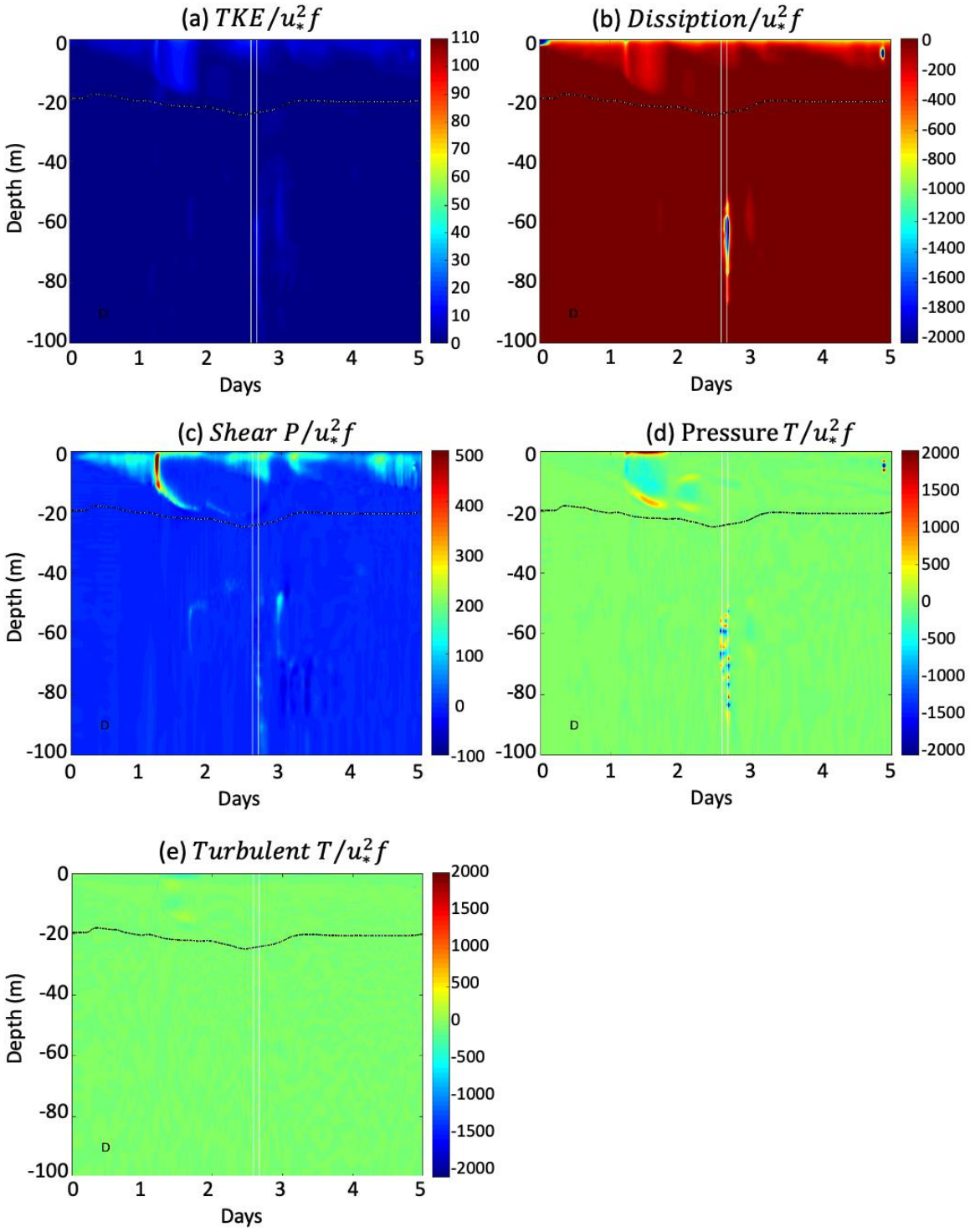

Figure VI.13. Normalized (a) TKE (e), (b) dissipation (ε), (c) shear production (ShearP), (d) pressure transport (PrsT), and (e) turbulent transport (TurT) at point C in simulation LES_KPP1. The black line is the MLD in the experiment, and the white dashed lines indicate simulation hour 24, 34 and 48 respectively as marked.

VII. Summary

NCOM, HYCOM and LES experiments are conducted to investigate the effect of submesoscale eddies on oceanic boundary layer turbulence through controlled numerical experiments conducted using the NCOM, HYCOM and the NCAR LES model. Idealized submesoscale eddy was initialized by a Gaussian surface pressure distribution with maximum surface geostrophic velocity following Penven et al. (2006) and imposed to the NCOM and HYCOM model domain for the experiments. Model experiments are performed with both moving and stationary eddy scenarios.

The different effect of the 6 OBL mixing models (KPP, GISS, MY 2.0, MY 2.5, Kantha-Clayson, and Harcourt) on the distortion of a submesoscale eddy and the corresponding responses of mixed layer dynamics are studied using stationary eddy experiments with NCOM and HYCOM. The turbulent mixing experiments in both models are setup such that the submesoscale eddy is initialized with a maximum current of 1 m/s and allowed to freely evolve. Sensitivity tests are performed with different turbulent mixing parameterizations in NCOM and HYCOM. Generally, for the second moment turbulent closure models, the mixed layer depth is deeper in the Mellor-Yamada and Mellor-Yamada 2.5 schemes but weakens much more quickly. While the Ramsey-Harcourt and Kantha-Clayson schemes result in an eddy that is stronger and more coherent but characterized by a shallower mixed layer (~22 m versus 30 m). In contrast to the second moment turbulent closure scheme, the KPP scheme produces weaker turbulent mixing with more symmetric structures and thus helps to better maintain the strength and coherence of the eddy. Preliminary analysis found that wind and wave forcing will lead to shallowing of the mixed layer at the center of the submesoscale eddies due to their impact on Ekman buoyancy flux and symmetric instability. These results demonstrate the important sensitivities of submesoscale eddy evolution to the application of the turbulent mixing scheme.

The interaction between submesocale eddies and OBL turbulence with a moving eddy are studied using HYCOM and LES simulations. An idealized submesoscale eddy is imposed to the HYCOM model domain with the eddy center position to be 25 km away from the domain center. Five locations along the middle cross section of the model domain and positioned at 10 km away from each other are selected for model results analysis. Two HYCOM simulations were conducted using the KPP and GISS mixing scheme respectively. Ten corresponding LES simulations were conducted at the five locations using the large scale gradient forcing and eddy forcing calculated form the two HYCOM simulations respectively.

We found that the mixed layer dynamics and the variation of the mixed layer depth (MLD) are very different at different locations relative to the eddy and between the HYCOM and LES simulations. Distinct dynamical processes are identified at different locations in the LES simulations. Along the center of the eddy, the turbulent field is dominated by strong shear production due to the geostrophic currents associated with the eddy, and the strong turbulent velocity fluctuations induced by the large horizontal shear brought by the eddy further act on the mean vertical shear to enhance the TKE and vertical mixing. On the right-hand side of the eddy, the mixed layer dynamics are dominated by the combined effect of Ekman buoyancy flux and geostrophic shear. While the Ekman buoyancy flux transports denser water over less dense water and results in convectively unstable state and destabilize the water column, the presence of geostrophic shear that is aligned with the wind-driven shear can also augment the wind-driven TKE generation that occurs through mechanical shear production. Both processes lead to enhanced

turbulence and deepening of the mixed layer. On the left-hand side of the eddy, however, the winds are aligned with the front such that denser water is to the right of the wind direction so that the Ekman buoyancy flux acts to be stabilizing, as it will transport lighter water over dense water and lead to stable stratification and shallowing of mixed layer.

The mixed layer in the HYCOM simulations do not show the strong deepening along the center and on the right-hand side of the eddy, or the shallowing on the left-hand side of the eddy as the LES simulations. This is because the Ekman buoyancy flux is not well represented in these HYCOM simulations, and the KPP and GISS parameterization used in the model can't represent the effect of horizontal gradients. Their mixing coefficient is a function of the surface boundary forcing and the state of the resolved velocity and potential density fields instantaneously in the water column. This means that these mixing schemes do not see the horizontal gradients, which, as demonstrated by the LES simulations, are the main source of turbulent mixing when the submesoscale eddy approaches the research locations.

Appendix A. Baroclinic Vortex Generation Code

```
  subroutine get_ic_bv(ind,n,m,l,r,e,u,v,zw,elon,alat)
c subroutine to set up the initial field for simulating a baroclinic vortex using Jei Yu's code and including
a Doppler shift to propagate the eddy
c
c      ind = flag to indicate if perturbation for internal wave is
c            to be included:  =0 no; =1 yes.
c      n,m,l = grid dimensions.  l = number of layers + 1.
c      r     = T and S fields.
c
      implicit none
c
c  declare passed variables.
      integer ind,n,m,l
      real*4  r(n,m,l-1,2),e(n,m),u(n,m,l-1),v(n,m,l-1)
      real*4  elon(n,m),alat(n,m),zw(l)
c
c  declare local temporary variables.
c
      integer i,j,k
      real*4 Nfreq,rho0,f0,lam,umax,h1,P0,Ome2,g
      real*4 a_f,fij,lam2,Fz,dFz,rhoij,x,y,eddy_sp
c
      g    = 9.81
      Ome2  = 2*7.292e-5              !2*Omega rad/sec
      Nfreq = 0.003                   !Brunt-Vaissala freq (1/sec), .003
      rho0  = 1025.0                  !mean density kg/m^3
      f0    = Ome2*sin(10.*3.1415/180.0) !f at 10.N
      lam   = 4.0e3/111.2e3           !e-folding scale in deg
      umax  = 1.                    !max surface geostrophic velocity m/sec
```

```
      h1    = 300                    !level of no-motion meter
c     eddy_sp = -10000./(24.*60.*60.)    !background advection of eddy
      eddy_sp = 0.0    !background advection of eddy
c
      lam2 = lam**2
      P0 = rho0*f0*umax*(lam*111.2e3)*sqrt(exp(1.0))
c
      if (ind .eq. 1) then
       do j=1,m
        do i=1,n
c          x=elon(i,j)-145.675 ! centered in model domain
ccar           x=elon(i,j)-(146.35-(50./111.2)) ! X km from right boundary
          x=elon(i,j)-(150.4-(300/111.2)) ! X km from right boundary
ccar           y=alat(i,j)-10.675  ! centered in model domain
          y=alat(i,j)-10.  ! centered in model domain
          a_f=exp( -(x**2+y**2)/(2.0*lam2) )
c         write(6,'(a,e14.4)') 'a = ', a
          fij=Ome2*sin(alat(i,j)*3.1415/180.0)
c Penven et al (2006)
c          e(i,j)=P0*a/(rho0*g-P0*a*(1.0-exp(-h1))/(h1-1.0+exp(-h1)))
c
c New function; see note 04-20-2018
          e(i,j)=P0*a_f/( rho0*g-P0*a_f*(exp(1.0)-1.0)/h1 )
c         write(6,'(e12.4)') e(i,j)
          do k=1,l-1
           if ( zw(k) > -h1 ) then
c Penven et al(2006)
c            Fz=P0*( h1-1.0+zw(k)+exp( -(zw(k)+h1) ) )
c   &           /( h1-1.0+exp(-h1) )
c            dFz=P0*( 1.0-exp(-(zw(k)+h1)) )/( h1-1.0+exp(-h1) )
c
c New function; see note 04-20-2018
             Fz =P0*(zw(k)/h1+exp( -(1.0+zw(k)/h1) ))*exp(1.0)
             dFz=P0*exp(1.0)/h1*(1.0-exp( -(1.0+zw(k)/h1)))
             rhoij = rho0*( 1.0-Nfreq**2*zw(k)/g )-dFz*a_f/g
             u(i,j,k)=-1.0/fij/rhoij*( -y/lam2/111.2e3 )*Fz*a_f
             u(i,j,k)= eddy_sp+u(i,j,k) ! add Doppler shift
             v(i,j,k)= 1.0/fij/rhoij*( -x/lam2/111.2e3 )*Fz*a_f
             r(i,j,k,1)=(1030-rhoij)/0.28
             r(i,j,k,2)=33.0-0.008*zw(k)
             if ( r(i,j,k,2) > 35.0) then
                      r(i,j,k,2)=35.0
             endif
ccar            r(i,j,k,2)= 35.0
            else
             rhoij = rho0*( 1.0-Nfreq**2*(-h1)/g )
             u(i,j,k)=0.0
             u(i,j,k)= eddy_sp+u(i,j,k) ! add Doppler shift
```

```
            v(i,j,k)=0.0
            r(i,j,k,1)= (1030-rhoij)/0.28
            r(i,j,k,2)=33.0-0.008*zw(k)
            if ( r(i,j,k,2) > 35.0) then
                        r(i,j,k,2)=35.0
            endif
ccar          r(i,j,k,2)= 35.0
          endif
         enddo
        enddo
       enddo
      endif

      if (ind .eq. 0) then  !get background T, S
       do j=1,m
        do i=1,n
        e(i,j)=0.0
         do k=1,l-1
          rhoij = rho0*( 1.0-Nfreq**2*zw(k)/g )
          r(i,j,k,1)= (1030-rhoij)/0.28
          r(i,j,k,2)=33-0.008*zw(k)
          if ( r(i,j,k,2) > 35.0) then
                      r(i,j,k,2)=35.0
          endif
ccar        r(i,j,k,2)= 35.0
          u(i,j,k)=0.0
          u(i,j,k)= eddy_sp+u(i,j,k) !add Doppler shift
          v(i,j,k)=0.0
         enddo
        enddo
       enddo
      endif
```

References:

Bleck, R. (2002). An oceanic general circulation model framed in hybrid isopycnic-Cartesian coordinates. Ocean Modelling, 4, 55–88. https://doi.org/10.1016/s1463-5003(01)00012-9

Blumberg, A.F. and G.L. Mellor, 1983: Diagnostic and prognostic numerical circulation studies of the South Atlantic Bight. J. Geophys. Res., 88, 4579- 4592.

Blumberg, A.F. and G.L. Mellor, 1987: A description of a three-dimensional coastal ocean circulation model. In Three-Dimensional Coastal Ocean Models, N. Heaps, Ed., American Union, New York, N.Y., 208 pp.

Canuto, V.M., Howard, A., Cheng, Y., Dubovikov, M.S., 2001. Ocean turbulence. Part I: one-point closure model. Momentum and heat vertical diffusivities. J. Phys. Oceanogr., 31, 1413–1426.

Canuto, V.M., Howard, A., Cheng, Y., Dubovikov, M.S., 2002. Ocean turbulence. Part II: vertical diffusivities of momentum, heat, salt, mass and passive scalars. J. Phys. Oceanogr., 32, 240–264.

Chassignet, E. P., Smith, L. T., Halliwell, G. R., & Bleck, R. (2003). North Atlantic simulations with the Hybrid Coordinate Ocean Model (HYCOM): Impact of the vertical coordinate choice, reference pressure, and thermobaricity. Journal of Physical Oceanography, 33, 2504–2526. https://doi.org/10.1175/1520-0485(2003)0332.0.CO;2

Craik, A. D. D., & Leibovich, S. (1976). A rational model for Langmuir circulations. J. FluidMech., 73, 401–426. doi:10.1017/S0022112076001420.

Fan, Y., Jarosz, E., Yu, Z., Rogers, E.W., Jensen, T.G., Liang, J.-H., 2018. Langmuir turbulence in horizontal salinity gradient. Ocean Modell. 129, 93–103. http://dx.doi.org/10.1016/j.ocemod.2018.07.010

Fan, Y., Z. Yu, I. Savelyev, P. P. Sullivan, J-H Liang, T. Haack, E. Terrill, T. de Paolo, K. Shearman, 2020. The effect of Langmuir turbulence under complex real oceanic and meteorological forcing. Ocean Modelling, 149, 101601. https://doi.org/10.1016/j.ocemod.2020.101601

Halliwell, G. R. (2004). Evaluation of vertical coordinate and vertical mixing algorithms in the HYbrid-Coordinate Ocean Model (HYCOM). Ocean Modelling, 7, 285–322. https://doi.org/10.1016/j.ocemod.2003.10.002.

Harcourt, R. R. 2015. A second-moment closure model of Langmuir turbulence. J. Phys. Oceanogr. 43:673–697

Kantha, L. H., and C. A. Clayson, 2004. On the effect of surface gravity waves on mixing in the oceanic mixed layer. Ocean Modell., 6, 101–124.

Kukulka, T., Plueddemann, A.J., Trowbridge, J.H., Sullivan, P.P., 2009. Significance of Langmuir circulation in upper ocean mixing: Comparison of observations and simulations. Geophys. Res. Lett. 36, L10603. http://dx.doi.org/10.1029/2009GL037620.

Large, W. G., McWilliams, J. C., & Doney, S. C. (1994). Oceanic vertical mixing—A review and a model with a nonlocal boundary-layer parameterization. Reviews of Geophysics, 32, 363–403. https://doi.org/10.1029/94rg01872

Liang, J.-H., Emerson, S.R., D'Asaro, E.A., McNeil, C.L., Harcourt, R.R., Sullivan, P.P., Yang, B., Cronin, M.F., 2017. On the role of sea-state in bubble-mediated air-sea gas flux during a winter storm. J. Geophys. Res. 122, 2671–2685.

Martin, P.J., G. Peggion, and K.J. Yip, 1998: A comparison of several coastal ocean models. NRL Report NRL/FR/7322--97-9692. Naval Research Laboratory, Stennis Space Center, Miss., 96 pp.

McWilliams, J. C., Sullivan, P. P., & Hoeng, C. (1997). Langmuir turbulence in the Ocean. J. Fluid Mech, 334, 1-30.

McWilliams, J. C., Restrepo, J. M., and Lane, E. M., 2004: An asymptotic theory for the interaction of waves and currents in coastal waters. J. Fluid Mech, 511, 135 – 178. DOI: 10.1017/S0022112004009358

McWilliams, J.C., Huckle, E., Liang, J-H. 2012: The Wavy Ekman Layer: Langmuir Circulations, Breaking Waves, and Reynolds Stress. J. Phys. Oceanogr. 42, 1973 – 1816.

McWilliams, J.C., Huckle, E., Liang, J.-H., Sullivan P.P., 2014. Langmuir turbulence in swell. J. Physical Oceanography, 44, 870-890. DOI: 10.1175/JPO-D-13-0122.1

Mellor, G. L, and T. Yamada 1982. Development of a turbulent closure model for geophysical fluid problmes. Reviews of geophysics and space physics, vol 20, no. 4, 851 – 875.

Mellor, G.L. and T. Yamada, 1974: A hierarchy of turbulence closure models for planetary boundary layers. J. Atmos. Sci., 31, 1791-1806.

Metzger, E. J., R.W. Helber, P.J. Hogan, P.G.Posey, P.G. Thoppil, T.L. Townsend, A.J. Wallcraft, O.M. Smedstad, and D.S. Franklin, 2017. Global Ocean Forecast System 3.1 Validation Testing. NRL Report NRL/MR/7320--17-9722, 59 pp. [Available from NRL, Code 7322, Bldg. 1009, Stennis Space Center, MS 39529-5004, USA].

Penven, P., Debreu, L., Marchesiello, P., and McWilliams, J. C., 2006: Evaluation and application of the ROMS 1-way embedding procedure to the central California upwelling system. Ocean Modelling, 12, 157 – 187.

Plumb, R. A., 1986: Three-dimensional propagation of transient quasi-geostrophic eddies and its relationship with the eddy forcing of the time-mean flow. J. Atmos. Sci., 43, 1657–1678.

Rowley C. and A. Mask, 2014: Regional and Coastal Prediction with the Relocatable Ocean Nowcast/Forecast System. Oceanography, 27, 3, doi:10.5670/oceanog.2014.67

Skyllingstad, E. D., Duncombe, J., and Samelson, R. M., 2017: Baroclinic Frontal Instabilities and Turbulent Mixing in the Surface Boundary Layer. Part II: Forced Simulations. J. Phys. Oceanogr., 47, 2429 – 2454. DOI: 10.1175/JPO-D-16-0179.1

Spall, M.A., Holland, W.R., 1991. A nested primitive equation model for oceanic applications. Journal of Physical Oceanography 21, 205–220.

Sullivan, P. P., McWilliams, J. C. & Moeng C.-H. (1996), A grid nesting method for large-eddy simulation of planetary boundary layer flows. Boundary-Layer Meteorol., **80**, 167-202.

Sullivan, P. P., McWilliams, J. C., & Melville, W. K. (2007). Surface gravity wave effects in the oceanic boundary layer: large-eddy simulation with vortex force and stochastic breakers. J. Fluid Mech. 593, 405-452. doi:10.1017/S002211200700897X

Sullivan, P. P. & Patton E. G. (2011). The effect of mesh resolution on convective boundary layer statistics and structures generated by large-eddy simulation. J. Atmos. Sci., **68**, 2395-2415.

Suzuki, N., Fox-Kemper B., 2016. Understanding Stokes forces in the wave-averaged equations, *J. Geophys. Res. Oceans*, **121**, 3579-3596, doi:10.1002/2015JC011566

Thomas, L. N., and C. M. Lee, 2005: Intensification of ocean fronts by down-front winds. J. Phys. Oceanogr., 35, 1086–1102, doi:10.1175/JPO2737.1.

Thomas, L. N., and J. R. Taylor , 2010: Reduction of the usable wind-work on the general circulation by forced symmetric instability. Geophys. Res. Lett., 37, L18606, https://doi.org/10.1029/2010GL044680.

Uchiyama, Y, McWilliams, J. C., & Shchepetkin, A. F. (2010). Wave–current interaction in an oceanic circulation model with a vortex-force formalism: application to the surf zone. Ocean Modelling, Doi: 10.1016/j.ocemod.2010.04.002

Wang, D., McWilliams, J. C. & Large, W. G. (1998). Large-eddy simulation of the diurnal cycle of deep equatorial turbulence. J. Physical Oceanography, 28, 129-148.